



# Highly selective and stable nickel catalysts supported on ceria promoted with $\text{Sm}_2\text{O}_3$ , $\text{Pr}_2\text{O}_3$ and $\text{MgO}$ for the $\text{CO}_2$ methanation reaction

G.I. Siakavelas<sup>a,b,c</sup>, N.D. Charisiou<sup>a</sup>, S. AlKhoori<sup>d</sup>, A.A. AlKhoori<sup>c,d</sup>, V. Sebastian<sup>e,f</sup>, S.J. Hinder<sup>g</sup>, M.A. Baker<sup>g</sup>, I.V. Yentekakis<sup>h</sup>, K. Polychronopoulou<sup>c,d,\*\*</sup>, M.A. Goula<sup>a,\*</sup>

<sup>a</sup> Laboratory of Alternative Fuels and Environmental Catalysis (LAFEC), Department of Chemical Engineering, University of Western Macedonia, GR-50100, Greece

<sup>b</sup> Department of Environmental Engineering, University of Patras, Agrinio, Greece

<sup>c</sup> Center for Catalysis and Separation, Khalifa University of Science and Technology, Abu Dhabi, P.O. Box 127788, United Arab Emirates

<sup>d</sup> Department of Mechanical Engineering, Khalifa University of Science and Technology, Abu Dhabi, P.O. Box 127788, United Arab Emirates

<sup>e</sup> Chemical and Environmental Engineering Department, Instituto De Nanociencia De Aragón (INA) and Instituto de Ciencia de Materiales de Aragón (ICMA), Universidad de Zaragoza-CSIC, 50018, Zaragoza, Spain

<sup>f</sup> Networking Research Center on Bioengineering, Biomaterials and Nanomedicine, CIBERBBN, 28029, Madrid, Spain

<sup>g</sup> The Surface Analysis Laboratory, Faculty of Engineering and Physical Sciences, University of Surrey, Guildford, GU2 4DL, UK

<sup>h</sup> Laboratory of Physical Chemistry & Chemical Processes, School of Environmental Engineering, Technical University of Crete, GR-73100, Chania, Greece

## ARTICLE INFO

### Keywords:

$\text{CO}_2$  methanation  
Ni catalysts  
Doped-Ceria support  
Oxygen vacant sites  
Microwave synthesis

## ABSTRACT

The present work reports on the investigation of the catalytic performance for the methanation of  $\text{CO}_2$  over Ni catalysts based on  $\text{CeO}_2$ , and for the first time, of Ni catalysts supported on binary  $\text{CeO}_2$ -based oxides, namely,  $\text{Sm}_2\text{O}_3$ - $\text{CeO}_2$ ,  $\text{Pr}_2\text{O}_3$ - $\text{CeO}_2$  and  $\text{MgO}$ - $\text{CeO}_2$ . The supports were obtained using the microwave assisted sol-gel method under reflux, while the catalysts were prepared by the wet impregnation method. For the investigation of the morphological, textural, structural and other intrinsic properties of the catalytic materials a variety of characterization techniques were used, i.e., Raman spectroscopy, XRD,  $\text{N}_2$  physisorption-desorption,  $\text{CO}_2$ -TPD,  $\text{H}_2$ -TPR,  $\text{H}_2$ -TPD, XPS and TEM. Carbon deposition and sintering were investigated using TEM. It was shown that the addition of  $\text{Sm}^{3+}$  or  $\text{Pr}^{3+}$ , incorporated into the lattice of  $\text{CeO}_2$ , generated oxygen vacancies, but the Ni/Pr-Ce catalyst was found to possess more surface oxygen vacancies (e.g.  $\text{Ce}^{4+}$ -Ov- $\text{Pr}^{3+}$  entities). Moreover, modification of  $\text{CeO}_2$  using  $\text{Sm}^{3+}$  or  $\text{Pr}^{3+}$  restricted the agglomeration of nickel active sites and led to the genesis of Lewis basic positions. These characteristics improved the hydrogenation reaction at lower temperature. On the other hand, the addition of  $\text{Mg}^{2+}$  resulted at strong metal support interactions reinforcing the resistance of the Ni/Mg-Ce catalyst against sintering. Furthermore, the addition of  $\text{Sm}^{3+}$ ,  $\text{Pr}^{3+}$  and  $\text{Mg}^{2+}$  cations increased the overall basicity and the moderate adsorption sites and led to the formation of smaller Ni nano particles; these physico-chemical properties enhanced the  $\text{CO}_2$  methanation reaction. Finally, the activity experiments (WGHSV = 25,000  $\text{mL g}^{-1} \text{h}^{-1}$ ,  $\text{H}_2/\text{CO}_2 = 4:1$ ,  $T = 350^\circ\text{C}$ ) showed that at lower reaction temperature the Ni/Pr-Ce had the highest catalytic performance in terms of  $\text{CO}_2$  conversion (54.5%) and  $\text{CH}_4$  yield (54.5%) and selectivity (100%). The TOF values were found to follow the order Ni/Pr-Ce > Ni/Mg-Ce > Ni/Sm-Ce > Ni/Ce.

## 1. Introduction

The catalytic hydrogenation of  $\text{CO}_2$  to  $\text{CH}_4$  (Sabatier reaction) can be performed at atmospheric pressure and temperature range between 200–400 °C and when using hydrogen derived from renewable energy sources (e.g. biomass or water electrolysis), can be considered sustainable [1,2]. The methane produced can be used as synthetic natural

gas in the residential sector, raw material in the chemical and petrochemical industries, fuel in private/public transportation and as energy carrier in the electricity sector, following well established methods for its storage and transfer [3,4]. Interest has also been expressed by the National Aeronautics and Space Administration (NASA) for the application of the Sabatier reaction in future manned space exploration for the colonization of Mars [5].

\* Corresponding author at: University of Western Macedonia, Department of Chemical Engineering, Laboratory of Alternative Fuels and Environmental Catalysis, Koila, Kozani, 50100, Greece.

\*\* Corresponding author at: Khalifa University of Science and Technology, Department of Mechanical Engineering, P O Box 127788, Abu Dhabi, United Arab Emirates.

E-mail addresses: [kyriaki.polychrono@ku.ac.ae](mailto:kyriaki.polychrono@ku.ac.ae) (K. Polychronopoulou), [mgoula@uowm.gr](mailto:mgoula@uowm.gr) (M.A. Goula).

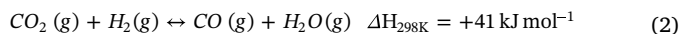
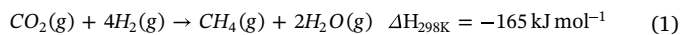
<https://doi.org/10.1016/j.apcatb.2020.119562>

Received 31 July 2020; Received in revised form 11 September 2020; Accepted 16 September 2020

Available online 21 September 2020

0926-3373/ © 2020 Elsevier B.V. All rights reserved.

According to the literature, CO<sub>2</sub> methanation (Eq. 1), a strongly exothermic reaction ( $\Delta H_{298K} = -165 \text{ kJ mol}^{-1}$ ), is performed via the intermediate production of CO through the reverse water-gas shift (RWGS) reaction (Eq. (2)), which is followed by CO hydrogenation to CH<sub>4</sub> (Eq. (3)) [6].



However, during the CO<sub>2</sub> hydrogenation process, and depending on the catalytic system and reaction condition used, part of the produced CO cannot participate in the hydrogenation reaction into CH<sub>4</sub>, resulting in low selectivity to CH<sub>4</sub> [7]. Thus, it is an urgent necessity to develop highly active catalytic systems, able to achieve efficiently the conversion of CO<sub>2</sub> to CH<sub>4</sub> at low reaction temperature ( $T < 400 \text{ }^\circ\text{C}$ ) with low CO production and high carbon resistance.

The methanation of CO<sub>2</sub> towards CH<sub>4</sub> can be performed over various noble and transition metal catalytic systems, such as Ru [8–10], Rh [11], Pd [12,13], Ir [14], Ni [5,15–21] and Co [22] based on different metal oxides and mesoporous materials (e.g., Al<sub>2</sub>O<sub>3</sub>, SiO<sub>2</sub>, CeO<sub>2</sub>, ZrO<sub>2</sub>, TiO<sub>2</sub>, MCM-41 and SBA-15). Noble metal based catalysts have been found to possess high activity for CO<sub>2</sub> methanation especially at low reaction temperatures, but their high cost makes them unattractive for industrial applications [23]. Ni based catalysts are also known to have high intrinsic activity, high CH<sub>4</sub> selectivity and relatively low cost [24,25], but can easily deactivate due to metal particle sintering and carbon formation on the catalyst surface [26,27].

Among the metal oxides and mesoporous materials that may be used as supports, cerium oxide, which has a typical fluorite structure, possesses a number of properties that can prove advantageous for the reaction at hand, i.e., (i) high oxygen storage capacity (OSC), (ii) redox properties (Ce<sup>4+</sup>/Ce<sup>3+</sup>) that help improve the dispersion of the active sites and decrease carbon deposition on the catalyst surface through carbon oxidation reactions, (iii) strong interaction with the supported metal (strong metal – support interaction), which can improve the stability of Ni nanoparticles against sintering, and (iv) increased basicity, which leads to the adsorption and activation of CO<sub>2</sub> on the support sites, providing more surface oxygen species and intermediate production of CO through the partial dissociation of CO<sub>2</sub>, which improves the CO hydrogenation to CH<sub>4</sub> [28–32]. A drawback is that cerium oxide suffers from limited thermal stability at elevated reaction temperatures [33].

The properties of CeO<sub>2</sub> can be further improved by the introduction of appropriate modifiers. According to the literature, the addition of rare-earth metals into the lattice of CeO<sub>2</sub> can improve its thermal stability and create additional oxygen vacancies; the latter are very useful in restricting the agglomeration of metal particles (e.g., Ni) [34–37]. Specifically, the formation of a solid solution with trivalent rare-earth cations (CeO<sub>2</sub>-Me<sub>2</sub>O<sub>3</sub> with Me = La, Sm, Gd, Pr, Y) causes an oxygen non-stoichiometry, which enhances O<sup>2-</sup> ion mobility [38]. Gomez-Sainero et al. [39] reported that the addition of Sm<sub>2</sub>O<sub>3</sub> into CeO<sub>2</sub>, forming a Ce-Sm-O solid solution, provided excellent thermal stability and good oxygen release/storage capacity, improving catalytic performance. It is generally accepted, that the formation of solid solution can be performed through the replacement of Ce<sup>4+</sup> sites of the cerium oxide lattice by trivalent cations (e.g., Sm<sup>3+</sup>, La<sup>3+</sup> and Pr<sup>3+</sup>) [40,41]. Furthermore, based on published studies, strongly basic material such as MgO can be used as additives in CeO<sub>2</sub> support, in order to induce promotional effects on the catalyst. Khajenoori et al. [42] reported that the simultaneous presence of CeO<sub>2</sub> and MgO on the catalyst surface was very effective in methane dry reforming as it helped achieve a relatively stable performance during time-on-stream experiments. Satio et al. [43] studied the performance of a Ru/MgO-CeO<sub>2</sub> (MgO:CeO<sub>2</sub> = 50:50 mol %) in ammonia synthesis and reported activity four times higher in comparison with a Ru/MgO catalyst.

Inspired from the above, a series of 10 wt% Ni loading catalysts were prepared using the wet impregnation technique. The supporting materials were CeO<sub>2</sub>, Pr<sub>2</sub>O<sub>3</sub>-CeO<sub>2</sub>, Sm<sub>2</sub>O<sub>3</sub>-CeO<sub>2</sub> and MgO-CeO<sub>2</sub> metal oxides, which were synthesized using the microwave assisted sol-gel method. The microwave technique has been extensively used for materials synthesis with higher reaction rates (reducing the reaction from hours to several minutes) in comparison with traditional hydro/solvothermal methods and its advantages have been dealt with in a number of impactful reviews [44–46]. Microwave synthesis has also been applied for the synthesis of ceria and ceria-based binary and ternary oxides with prominent oxidation [33,35,40,47] and reforming [41] activity due to the degree of homogeneity achieved in complex composition systems.

To the best of our knowledge, this is the first time that ceria promoted with Sm<sub>2</sub>O<sub>3</sub>, Pr<sub>2</sub>O<sub>3</sub> or MgO have been used as supporting material for Ni based catalysts in the CO<sub>2</sub> methanation reaction. Moreover, this is also the first time that this particular support preparation method has been used for the reaction at hand. To investigate the catalytic surface and bulk properties, calcined, reduced and used catalytic samples were characterized using different techniques such as Raman spectroscopy, X-Ray Diffraction (XRD), N<sub>2</sub> adsorption/desorption, CO<sub>2</sub> Temperature Programmed Desorption (TPD-CO<sub>2</sub>), H<sub>2</sub> Temperature Programmed Reduction (TPR-H<sub>2</sub>), H<sub>2</sub> Temperature Programmed Desorption (TPD-H<sub>2</sub>), X-ray Photoelectron Spectroscopy (XPS) and Transmission Electron Microscopy (TEM). The study of the catalytic performance was carried out in order to investigate the effect of temperature and molar ratio of the reactants on: (i) carbon dioxide conversion, (ii) carbon monoxide and methane selectivity and (iii) methane yield. Moreover, time on steam experiments were performed in order to investigate carbon deposition and the possible agglomeration of Ni particles.

## 2. Experimental

### 2.1. Support and catalyst preparation

CeO<sub>2</sub> and M<sub>x</sub>O<sub>y</sub>-CeO<sub>2</sub> (M = Sm<sup>3+</sup>, Pr<sup>3+</sup>, Mg<sup>2+</sup>) promoted supports were synthesized by a microwave assisted sol-gel method using a microwave accelerated reaction system (MARS-6) with a power output of 0–1800 W ± 5% (IEC 705 Method-1988). The microwave reaction system was described in detail previously [33]. The metal nitrates Ce(NO<sub>3</sub>)<sub>3</sub> 6H<sub>2</sub>O (Aldrich, 99.95%), Sm(NO<sub>3</sub>)<sub>3</sub> 6H<sub>2</sub>O (Aldrich, 99.95%), Pr(NO<sub>3</sub>)<sub>3</sub> 6H<sub>2</sub>O (Aldrich, 99.95%) and Mg(NO<sub>3</sub>)<sub>2</sub> 6H<sub>2</sub>O (Aldrich, 99.95%) were used as precursors. During the process, 0.06 mol of the metal salts (nominal molar ratio Ce:M = 0.9:0.1) were dissolved in 300 mL of a mixture of 66.7 vol.% ethylene glycol in water, under continuous stirring at room temperature (RT). The metal salt and ethylene glycol mixture were subjected to microwave heating (130 °C/800 W) and stirring until a yellowish gel was formed. The solutions were then stirred at RT for 2 h where the formation of precipitate was noticed. Following microwave synthesis, all samples were dried at 120 °C for 12 h and calcined at 500 °C for 6 h under atmospheric conditions to form the oxide and mixed oxide samples.

Metal supported catalysts were prepared in a second synthesis step following a wet impregnation procedure where the appropriate concentration of Ni(NO<sub>3</sub>)<sub>2</sub> 6H<sub>2</sub>O (Chem-Lab ≥ 96%) aqueous solution was used in order to obtain catalysts with a Ni loading of about 10 wt.%. After impregnation, the materials obtained were air dried overnight at 120 °C and calcined at 400 °C for 6 h; these samples are denoted throughout this manuscript as “calcined” samples. Reduced catalysts were also produced by reduction at 500 °C for 1 h under a flow of pure H<sub>2</sub>. Finally, the supports used herein were labelled as Ce, Sm-Ce, Pr-Ce and Mg-Ce and the catalytic samples as Ni/Ce, Ni/Sm-Ce, Ni/Pr-Ce and Ni/Mg-Ce.

### 2.2. Materials characterization

The surface area and porosimetry were analyzed using the 3Flex (Micromeritics, USA), recording isothermal curves of N<sub>2</sub> adsorption/desorption (at –196 °C, recorded manometrically up to 1 bar).

Specifically, total Specific Surface Area (SSA) was determined by the multi-point Brunauer-Emmet-Teller (BET) method in the relative pressure range  $0.05 < P/P_0 < 0.20$ . Pore Size Distribution (PSD) was estimated by the BJH Theory.

The crystal phases and the crystalline structure was characterized at room temperature (RT) by applying the X-ray diffraction (XRD) technique, using a Rigaku MiniFlex II powder diffraction system (Rigaku, Tokyo, Japan) with Cu-K $\alpha$ 1 radiation operated at 30 kV and 20 mA. The identification of the diffraction pattern was performed according to the International Center for Diffraction Data (ICDD) database. The Scherrer equation (Eq. (4)) was used in order to determine the particle size of the various phases, based on their strongest reflection.

$$L = \frac{0.9 * \lambda}{\beta * \cos \theta} \quad (4)$$

where  $L$  is the width of the crystallite (nm),  $\lambda$  is the wave length of incident radiation (1.5418 Å),  $\beta$  is the half-height width of the most intense peak for the species (radians), and  $\theta$  is the Bragg angle ( $^\circ$ ) of that peak.

CO<sub>2</sub> Temperature Programmed Desorption (TPD-CO<sub>2</sub>) experiments for the investigation of acid-base properties were performed using the Autochem 2920 apparatus (Micromeritics, Atlanta, USA). The CO<sub>2</sub>-TPD experiments were performed over the Ni-supported catalysts following their reduction at 500 °C for 1 h. Succinctly, a gas mixture of 5 vol% CO<sub>2</sub>/Ar was passed over 0.12 g of the calcined (20 vol% O<sub>2</sub>/He, 500 °C, 2 h) catalyst using a temperature ramp of 30 °C/min, while the Thermal Conductivity Detector (TCD) signal was recorded continuously.

The reducibility of the catalytic samples was investigated by H<sub>2</sub> temperature-programmed reduction (H<sub>2</sub>-TPR). In short, the TPR experiments were conducted using the Autochem 2920 apparatus (Micromeritics, Atlanta, USA) by passing 10 vol% H<sub>2</sub>/Ar gas mixture over 0.12 g of the calcined (20 vol% O<sub>2</sub>/He, 500 °C, 2 h) catalyst, using a temperature ramp of 30 °C/min, while the TCD signal was recorded continuously.

H<sub>2</sub>-TPD experiments were performed in a quartz fixed-bed reactor. The methodology used is being described in the supplementary information (SI) file and followed closely the one reported in ref. [48]. The H<sub>2</sub> signal ( $m/z = 2$ ) was continuously monitored with an on-line mass spectrometer (QMS 200 Prisma Quadrupole Mass Spectrometer) and converted into concentration (ppm).

The morphological characteristics of the reduced and spent catalytic samples were examined by Transmission Electron Microscopy (TEM), using a 200 kV G2 20 S-Twin Tecnai microscope with a LaB6 electron source fitted with a "SuperTwin" objective lens allowing a point to point resolution of 0.24 nm. Energy dispersive X-ray spectroscopy (EDS) analysis and high angle annular dark field scanning transmission electron microscopy (STEM-HAADF) were performed on a Tecnai G2-F30 Field Emission Gun microscope with super-twin lens and 0.2 nm point-to-point resolution and 0.1 nm line resolution operated at 300 kV.

XPS analyses were performed on a ThermoFisher Scientific Instruments (East Grinstead, UK) K-Alpha + spectrometer. XPS spectra were acquired using a monochromated Al K $\alpha$  X-ray source ( $h\nu = 1486.6$  eV). An X-ray spot of  $\sim 400$   $\mu$ m radius was employed. Survey spectra were acquired employing a Pass Energy of 200 eV. High resolution, core level spectra for all elements were acquired with a Pass Energy of 50 eV. All spectra were charge referenced against the C1 s peak at 285.0 eV to correct for charging effects during acquisition. Quantitative surface chemical analyses were calculated from the high resolution, core level spectra following the removal of a non-linear (Shirley) background. The manufacturers Advantage software was used, which incorporates the appropriate sensitivity factors and corrects for the electron energy analyzer transmission function.

Complementary structural information such as oxygen sublattice were received using Witec Alpha 300 Raman spectroscopy (Germany) that is equipped with 532 nm laser and research grade optical microscope with various lenses. The instrument features a manual sample positioning with both planar (x,y-direction) and depth scans (z-direction). All the catalysts spectra were acquired using single-point Raman spectrum acquisition. The Raman spectra were collected over both the

calcined supports and the Ni supported catalysts following their reduction at 500 °C for 1 h.

### 2.3. Catalytic tests

The catalytic activity tests were performed at atmospheric pressure, using a continuous flow fixed-bed tubular reactor (reactor I.D. = 0.9 cm, catalyst loading  $w_{\text{cat}} = 0.240$  g). A cold trap was employed at the reactor outlet to remove the produced water vapour during the reaction. Before catalytic evaluation measurements, all catalysts were in situ activated for 1 h at 500 °C under a flow of pure H<sub>2</sub>. The catalytic evaluation tests were performed using three experimental protocols (#1, #2 and #3).

Experimental protocol #1 was designed with the purpose of investigating the effect of the reaction temperature on CO<sub>2</sub> conversion, CO and CH<sub>4</sub> selectivity and CH<sub>4</sub> yield in the temperature range of 200–500 °C at a Weight-basis Gas Hourly Space Velocity (WGHSV) of 25,000 mL g<sup>-1</sup> h<sup>-1</sup>; the total flow rate used was 100 mL min<sup>-1</sup>. The gas mixture used as feedstock consisted of 10% CO<sub>2</sub>, 40% H<sub>2</sub> and 50% Ar, corresponding to a H<sub>2</sub>/CO<sub>2</sub> molar ratio equal to 4, i.e., at the stoichiometry of the methanation reaction (Eq.1). After the reduction process, the temperature of the catalytic bed was retained at 500 °C under a flow of pure Ar for 30 min. Then the reaction mixture was introduced into the reactor and the temperature was decreased stepwise (50 °C steps), remaining for 30 min at each temperature in order to ensure reaction conditions at steady-state operation. Experimental protocol #2 was designed with the purpose of investigating catalytic stability during 20 h time-on-stream (again, H<sub>2</sub>/CO<sub>2</sub> = 4/1, WGHSV = 25,000 mL g<sup>-1</sup> h<sup>-1</sup>). Stability was tested at 400 °C and the experimental procedure followed was similar to that described above. Finally, for experimental protocol #3, the H<sub>2</sub>/CO<sub>2</sub> molar ratio was reduced to 3/1 and short stability experiments lasting for 7 h were performed, with the purpose of investigating activity at less advantageous reaction conditions (T = 400 °C, WGHSV = 25,000 mL g<sup>-1</sup> h<sup>-1</sup> and H<sub>2</sub>/CO<sub>2</sub> ratio less than the methanation reaction stoichiometry). For both experimental protocols #2 and #3, activity measurements were taken every hour. CO<sub>2</sub> conversion, CO or CH<sub>4</sub> selectivity and CH<sub>4</sub> yield during catalytic evaluation were determined according to the following equations (Eqs. 5–8):

$$X_{\text{CO}_2} = \frac{F_{\text{CO}_2}^{\text{in}} - F_{\text{CO}_2}^{\text{out}}}{F_{\text{CO}_2}^{\text{in}}} \times 100\% \quad (5)$$

$$S_{\text{CH}_4} = \frac{C_{\text{CH}_4}^{\text{out}}}{C_{\text{CO}}^{\text{out}} + C_{\text{CH}_4}^{\text{out}}} \times 100\% \quad (6)$$

$$S_{\text{CO}} = \frac{C_{\text{CO}}^{\text{out}}}{C_{\text{CO}}^{\text{out}} + C_{\text{CH}_4}^{\text{out}}} \times 100\% \quad (7)$$

$$Y_{\text{CH}_4} = \frac{X_{\text{CO}_2} * S_{\text{CH}_4}}{100} \quad (8)$$

where  $F^{\text{in}}$  and  $F^{\text{out}}$  represent the molar flow rate of CO<sub>2</sub> in the inlet/outlet of the reactor and  $C^{\text{out}}$  is the concentration of each component in the outlet of the reactor.

The reactor outlet composition was analyzed online by gas chromatography using an Agilent 7890A (Agilent Technologies, California, USA) with He carrier gas equipped with thermal conductivity detector (TCD) and flame ionization detector (FID) and two columns in parallel, Agilent J&W HP Plot-Q (19095-Q04, 30 m length, 0.530 mm I.D.) and Agilent J&W HP-Molesieve (19095P-MSO, 30 m length, 0.530 mm I.D.).

The intrinsic reaction rates were measured under differential reaction conditions, i.e., for conversions of reactants lower than 15% (specifically, WGHSV = 100,000 mL g<sup>-1</sup> h<sup>-1</sup>, weight of catalyst = 0.06 g). These results, along with the measurements of metal dispersion, were used to calculate the turnover frequencies (TOFs) of carbon dioxide conversion, defined as moles of CO<sub>2</sub> converted per moles of surface nickel metal atom per second (s<sup>-1</sup>). The equations used are described in the SI.

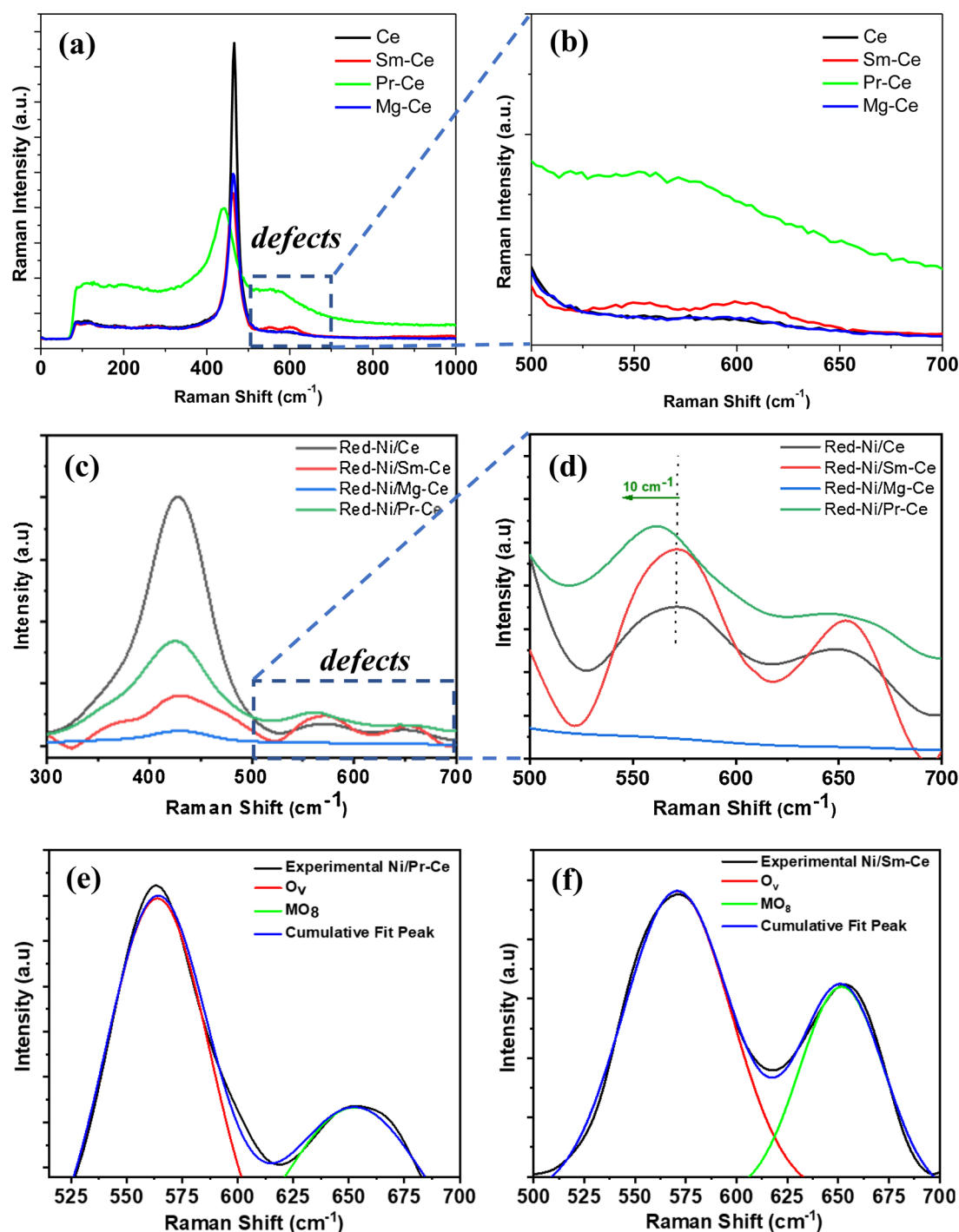


Fig. 1. (a and b) Raman spectra of the calcined supporting materials, and (c and d) Raman spectra of the reduced Ni/Ce, Ni/Sm-Ce, Ni/Pr-Ce and Ni/Mg-Ce catalysts.

### 3. Results and discussion

#### 3.1. Raman analysis

Fig. 1 presents the Raman spectra acquired over the calcined supports (Fig. 1a, b) and the Ni catalysts (Fig. 1c, d) following their reduction at 500 °C for 1 h, with particular emphasis on the 500–600  $\text{cm}^{-1}$  region for the supports (Fig. 1b) and the Ni catalysts (Fig. 1d), respectively. In addition, Figs. 1(e) and 1(f) present the deconvoluted Raman spectra in the defects' region (500–650  $\text{cm}^{-1}$ ) as obtained over the reduced Ni/Pr-Ce and Ni/Sm-Ce catalysts, respectively.

Discussing the supporting materials first, in the case of  $\text{CeO}_2$ , one sharp Raman band is observed at 464  $\text{cm}^{-1}$  which is assigned to the F2g

vibration of the fluorite lattice (F-type of structure) [40] (Fig. 1a). This peak corresponds to the oxygen ions in  $\text{CeO}_8$  entities, i.e. oxygen around the cerium cations in eightfold coordination in good agreement with the literature [49]. Upon doping with  $\text{Sm}^{3+}$ ,  $\text{Pr}^{3+}$  and  $\text{Mg}^{2+}$  a red shift of the F2g peak with a simultaneous lowering in intensity can be noticed, which is more pronounced in the case of  $\text{Pr}^{3+}$  (Fig. 1a). These new features of the F2g peak are indicative of the formation of a solid solution [49,50]. Furthermore, doping induces the generation of defects in the structure (defects region). The Raman band at 600  $\text{cm}^{-1}$  can be attributed to the dopant in eightfold coordination environment (e.g.  $\text{PrO}_8$ ,  $\text{SmO}_8$ ) and does not contain contribution from oxygen vacancies, whereas the peak at 540  $\text{cm}^{-1}$ , clearly observed here in the case of  $\text{Pr}^{3+}$  and  $\text{Sm}^{3+}$  doped systems, corresponds to oxygen vacancies ( $\text{O}_v$ )

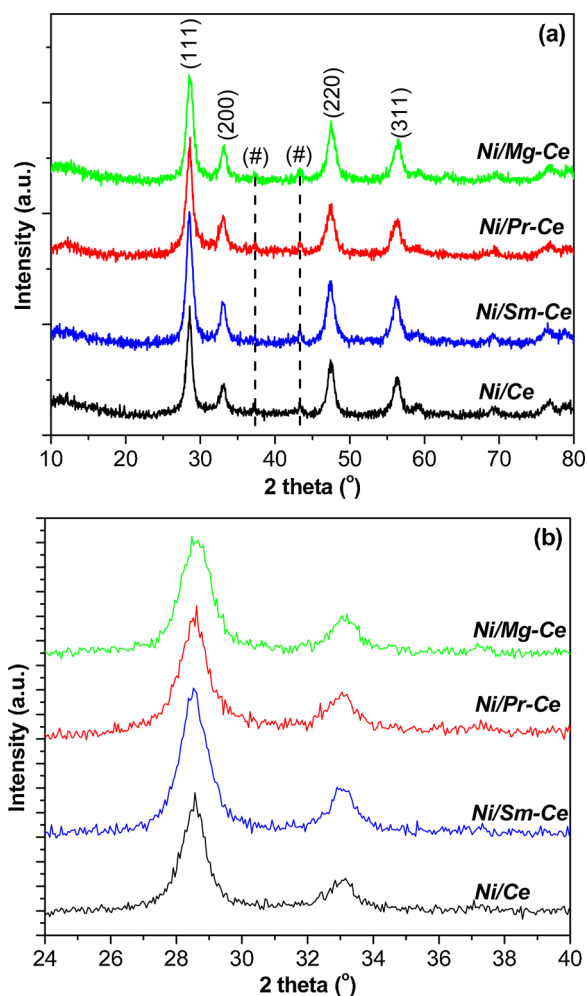


Fig. 2. (a and b) XRD patterns of the calcined Ni/Ce, Ni/Sm-Ce, Ni/Pr-Ce and Ni/Mg-Ce catalysts.

(Fig. 1b), generating Lewis basic positions, which strongly adsorb and dissociate the gaseous  $\text{CO}_2$  improving the hydrogenation reaction at lower temperature [51–53]. The oxygen vacancies are formed by the  $\text{Ce}^{4+}$  substitution from  $\text{Pr}^{3+}$  or  $\text{Sm}^{3+}$ . It is very interesting that this peak ( $540\text{ cm}^{-1}$ ) has completely vanished in the case of pure  $\text{CeO}_2$  (non-doped) and  $\text{Mg}^{2+}$  doped  $\text{CeO}_2$ , a result that corroborates for the absence of  $\text{O}_v$  formation upon  $\text{Mg}^{2+}$  doping. Taking into consideration the ionic radius of the elements of interest, namely  $\text{Sm}^{3+}$  ( $1.02\text{ \AA}$ ),  $\text{Pr}^{3+}$  ( $1.13\text{ \AA}$ ),  $\text{Ce}^{4+}$  ( $0.97\text{ \AA}$ ) and  $\text{Mg}^{2+}$  ( $0.72\text{ \AA}$ ), the ionic radii difference  $\text{Ce-X}$ , ( $\text{X} = \text{Sm}^{3+}$ ,  $\text{Pr}^{3+}$ ,  $\text{Mg}^{2+}$ ) is 5.2%, 16.5% and 25.8%, respectively. According to the Hume-Rothery rules [54], when the difference is up to 15% substitutional solid solution can be formed. So, it is expected that in the case of  $\text{MgO}$  low solubility in the  $\text{CeO}_2$  lattice is achieved preserving the two phases ( $\text{MgO}$  and  $\text{CeO}_2$ ) as separate ones.

In the case of the Ni supported catalysts, the Raman spectra were collected following the reduction of the catalysts so as to resemble the surface condition just before the reaction. The defect region (Fig. 1d) can be analyzed using the contributions from the oxygen vacant sites ( $\text{O}_v$ ) and the impurity phase ( $\text{MO}_8$ , where M stands for Sm, Pr) (Figs. 1e,f). It is observed that in the case of Mg-doping the  $\text{O}_v$  peak is vanishing and this is due to  $\text{O}_v$  annihilation due to the interstitially (most likely) located  $\text{Mg}^{2+}$  ions. The absence of  $\text{O}_v$  in the case of  $\text{Mg}^{2+}$ -doping was also observed in the case of the oxides only (see above). On the contrary, in the case of Ni/ $\text{CeO}_2$  catalyst there is an  $\text{O}_v$  band, whereas in the ceria alone only a weak  $\text{O}_v$  band can be noticed. Additionally, Sm- and Pr- doping of the Ni catalysts, leads to the formation of  $\text{O}_v$  with a distinct peak (Fig. 1c & d). The  $\text{O}_v/\text{F}_{2g}$  ratio is considered as a descriptor of the vacant sites

population; the values of the  $\text{O}_v/\text{F}_{2g}$  ratio were found to be 0.09, 0.6 and 0.3 for the Ni/Ce, Ni/Sm-Ce and Ni/Pr-Ce catalysts. These results can be understood on the basis of the local structure study as reported by Nitani et al. [55] using EXAFS. Specifically, Nitani et al. concluded that Pr-induces lower amount of  $\text{O}_v$  compared to Sm and this has to do with the fact that Ce and Pr coordination numbers (CN) are similar; Pr can host eight oxygen atoms as exactly Ce does; both of them exist in 3+ and 4+ oxidation state. On the other hand, Sm exists in 3+ oxidation state and has different CN than Ce, leading to the formation of  $\text{O}_v$ .

The role of oxygen vacancies in the  $\text{CO}_2$  hydrogenation reaction is pivotal; they react with the  $\text{CO}_2$ , weakening the  $\text{C}=\text{O}$  bond and boosting the reaction at lower temperatures. Also, it is noteworthy that, according to the data presented in Fig. 1(d), there is an insignificant shift in the Sm-doped catalyst defect band, whereas a big shift of  $10\text{ cm}^{-1}$  is noticed in the Pr-doped one, when both are compared to the Ni/Ce catalyst' defect band. This shift corroborates with a high disturbance of the  $\text{O}_v$  environment and a possible formation of associated (cluster) defects [56,57]. Also, another feature to be taken into consideration is not only the amount but also the location of the  $\text{O}_v$  as this is indicated by the peak at  $250\text{ cm}^{-1}$  (not shown) which was observed only for the Pr-containing catalyst and suggests the presence of  $\text{O}_v$  at the surface [58].

### 3.2. Crystal structure and adsorption isotherms

The XRD diffraction patterns showing the crystalline composition of each catalytic sample are presented in Fig. 2(a), while Fig. 2(b) focuses on  $2\theta = 25\text{--}40^\circ$ . For all catalysts, the polycrystalline ceria fluorite structure is clearly observed through the presence of sharp diffraction peaks (i.e.,  $2\theta = 28.5^\circ$  for plane (111),  $2\theta = 33.0^\circ$  for plane (200),  $2\theta = 47.3^\circ$  for plane (220), and  $2\theta = 56.3^\circ$  for plane (311) [59]. Moreover, two small peaks at  $37.3^\circ$  and  $43.2^\circ$ , present in the diffractogram correspond to the (111) and (200) planes of the NiO cubic structure (JCPDS card no. 96-900-8694).

As can be observed from Fig. 2b, the (111) diffraction peak at  $2\theta = 28.5^\circ$  of the Ni/Sm-Ce and Ni/Pr-Ce catalytic systems has been slightly shifted to lower diffraction angles in comparison with the pure ceria-based catalyst. The shift to lower angles is associated with an increase in the lattice parameters resulting from the incorporation of the larger  $\text{Sm}^{3+}$  and  $\text{Pr}^{3+}$  ions into the cerium oxide crystal lattice, in agreement with other literature reports [41]. In the case of Ni/Mg-Ce catalyst, the addition of 10 at. % Mg does not result in any shift of the (111) diffraction peak, indicating that the much smaller Mg ions are not being incorporated into the  $\text{CeO}_2$  lattice and are most probably forming a separate amorphous or highly dispersed  $\text{MgO}$  phase, in good agreement with the Raman studies, previously discussed.

For all catalysts, the crystallite sizes, have been calculated using the Scherrer formula and are determined from the strongest (111) reflection at  $28.5^\circ$  (Table 1). For the doped catalysts, the crystallite sizes of  $\text{CeO}_2$  were found between of 7.8–8.7 nm, smaller than that of the undoped catalyst ( $\approx 11\text{ nm}$ ), as expected. In the case of Ni/Ln-Ce (Ln =  $\text{Sm}^{3+}$ ,  $\text{Pr}^{3+}$ ), the decrease of the  $\text{CeO}_2$  crystallite size is an indication of solid solution formation, which confirms the incorporation of the above trivalent cations into the lattice of  $\text{CeO}_2$ . On the other hand, regarding the Ni/Mg-Ce catalyst, the small particle size (7.8 nm) can be explained based on the hypothesis that the addition of  $\text{Mg}^{2+}$  is causing the formation of a separate phase, and the decrease of  $\text{CeO}_2$  crystallite size is due to the competitive growth of the two separate phases ( $\text{MgO}$  against  $\text{CeO}_2$ ). Moreover, as can be observed in Table 1, the addition of dopants also resulted in smaller nickel particle sizes, which followed the order Ni/Mg-Ce (12.5 nm) < Ni/Pr-Ce (15.1 nm) < Ni/Sm-Ce (18.7 nm) < Ni/Ce (22.8 nm), possibly due to interaction/synergism between Ni-support [60]. As is well established, smaller metal particles improve the dispersion of active sites and lead to higher catalytic activity and selectivity in terms of the desired gaseous products. It is also worthwhile to mention that the smallest Ni particle size (12.5 nm) is achieved in the case of the smallest support size (Mg-Ce: 7.8 nm). This demonstrates the better Ni

**Table 1**  
Textural properties of the Ni/Ce, Ni/Sm-Ce, Ni/Pr-Ce and Ni/Mg-Ce catalysts.

Catalyst	BET ( $\text{m}^2/\text{g}$ )	Pore volume ( $\text{cm}^3/\text{g}$ )	Average Pore width (nm)	CeO <sub>2</sub> particle msze <sup>1</sup> (nm)	NiO particle size <sup>1</sup> (nm)	Ni <sup>0</sup> particle size <sup>2</sup> (nm)
Ni/Ce	42.7	0.12	20	10.8	22.8	4.4 ± 1.5
Ni/Sm-Ce	45.8	0.08	18	8.7	18.7	3.6 ± 1.3
Ni/Pr-Ce	50.1	0.10	20	9.9	15.1	3.4 ± 1.0
Ni/Mg-Ce	48.1	0.11	18	7.8	12.5	3.7 ± 1.2

Note: <sup>1</sup>Calculated by the Scherrer formula, <sup>2</sup>Calculated by the TEM analysis.

dispersion on the smallest crystallite size support and allows us to speculate for stronger metal-support interactions due to the finer interface.

The specific surface area ( $\text{m}^2\text{g}^{-1}$ ), pore volume ( $\text{cm}^3\text{g}^{-1}$ ) and average pore width (nm) of the supporting material and catalysts used herein are presented in Table 1. As expected, the specific surface area recorded for the supporting materials (Ce =  $59.0\text{ m}^2\text{g}^{-1}$ , Sm-Ce =  $68.5\text{ m}^2\text{g}^{-1}$ , Pr-Ce =  $67.8\text{ m}^2\text{g}^{-1}$  and Mg-Ce =  $71.5\text{ m}^2\text{g}^{-1}$ ) was higher in comparison to that of the catalytic samples (i.e., after the introduction of the Ni particulates) (Ni/Ce =  $42.7\text{ m}^2\text{g}^{-1}$ , Ni/Sm-Ce =  $45.8\text{ m}^2\text{g}^{-1}$ , Ni/Pr-Ce =  $50.1\text{ m}^2\text{g}^{-1}$  and Ni/Mg-Ce =  $48.1\text{ m}^2\text{g}^{-1}$ ) however, the catalytic samples did not present significant differences between them (Table 1). The decrease in the specific surface area is due to the nickel particulates covering of the internal surface area of the support pore system blocking the micropores [61]. According to the International Union of Pure and Applied Chemistry (IUPAC) classification the synthesized catalytic materials present type IV isotherms [62]. Fig. 3 present the N<sub>2</sub> adsorption/desorption isotherms curves and the pore size distribution for the catalytic samples. As can be observed, there is a small hysteresis loop in the P/P<sub>0</sub> adsorption and desorption range of 0.45–0.80, which can be related with capillary condensation of N<sub>2</sub> gas inside the mesopore structures [63]. Furthermore, at the maximum P/P<sub>0</sub> point of  $\approx 0.99$  the N<sub>2</sub> isotherms extend in an almost vertical direction due to the typical macropore structures of the catalytic samples (i.e., pore sizes above 50 nm) [62], which can be confirmed by the corresponding pore size distribution.

### 3.3. Basic properties (TPD-CO<sub>2</sub>)

CO<sub>2</sub>-TPD experiments (Fig. 4) for all catalytic samples (after pretreatment in hydrogen atmosphere) were carried out to determine: (i) the surface basic sites and (ii) the way in which the CO<sub>2</sub> molecule dynamically interacts with the catalyst surface. In general, it is well known that the CO<sub>2</sub> adsorption/desorption is associated with the strength of basic sites on the catalytic surface [64]. As can be observed from Fig. 4, all the catalytic samples show similar desorption peaks, which can be divided into three adsorption parts corresponding to three kinds of sites with different basic characters. The first 'region' located at lower adsorption temperature ( $< 200\text{ }^\circ\text{C}$ ) can be assigned to weak basic sites, the second adsorption region ( $200\text{--}400\text{ }^\circ\text{C}$ ) can be attributed to moderate basic sites, while the third adsorption region at higher temperature ( $> 400\text{ }^\circ\text{C}$ ) can be ascribed to high strength basic sites and/or decomposition of carbonates which were not eliminated during the calcination process [65,66]. According to the literature [67], the moderate adsorption sites are active for CO<sub>2</sub> methanation, while the weak adsorption and strong adsorption sites are inactive for CO<sub>2</sub> methanation. Specifically, the weak basic sites are not sufficiently active to break the chemical bonds, whereas the strong basic sites make the reaction products hard to be desorbed [68].

In order to interpret the CO<sub>2</sub>-TPD results and correlate them with the catalytic activity in the CO<sub>2</sub> hydrogenation, fundamentals of CO<sub>2</sub> adsorption as well as ceria surface–CO<sub>2</sub> activation should be discussed. The defect chemistry of ceria is known to affect the CO<sub>2</sub> adsorption, as it has been proved by experimental and theoretical studies. According to the literature [69,70], the CO<sub>2</sub> adsorption follows a similar trend with the oxygen vacant sites (defect sites). Defect sites are usually

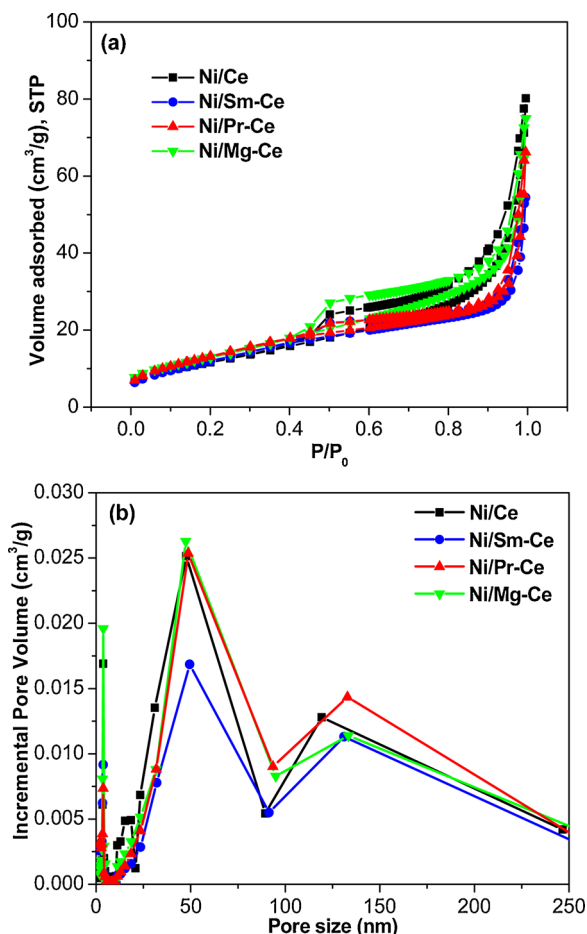


Fig. 3. (a) N<sub>2</sub> adsorption-desorption isotherms and (b) pore size distribution of the calcined Ni/Ce, Ni/Sm-Ce, Ni/Pr-Ce and Ni/Mg-Ce catalysts.

located at the surface, subsurface and bulk; those at the surface are the most significant ones for the CO<sub>2</sub> adsorption. Doping of ceria is beneficial for the CO<sub>2</sub> adsorption as, according to Staudt et al. [69] the CO<sub>2</sub> activation on undoped CeO<sub>2</sub> can lead to the rapid formation of a carbonate and surface carboxylates. On the other hand, doping of ceria can tune the redox and acid-basic properties as well as the oxygen vacancies population. Theoretical (ab initio) studies showed that CO<sub>2</sub> adsorption on reduced CeO<sub>2</sub> (110) is thermodynamically favoured compared to stoichiometric CeO<sub>2</sub> (110), whereas the most favorable CO<sub>2</sub> configuration is that of CO<sub>2</sub> approaching parallel to the reduced CeO<sub>2</sub> (110) surface, and being adjacent to the oxygen vacancy. During the activation, the O-C-O angle reaches  $136.9^\circ$  while the C-O elongates and a total charge of  $-0.955e$  is transferred from the reduced ceria to the CO<sub>2</sub> molecule (attracted mostly by the oxygen) [70]. As it can be observed from Fig. 4, the overall basicity of the Pr-doped catalyst is much higher in comparison with the other samples used herein. In order to draw some semi-qualitative results, the areas of the CO<sub>2</sub> desorption peaks were calculated and were found to follow the order: Ni/Pr-Ce > Ni/Mg-Ce > Ni/Ce > Ni/Sm-Ce.

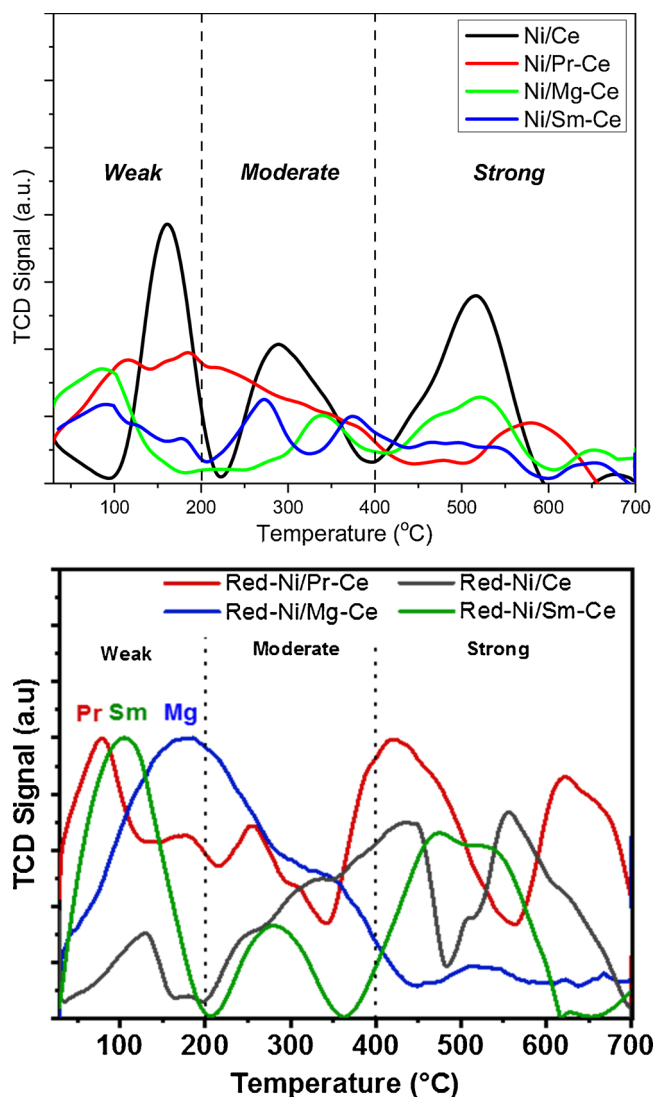


Fig. 4. CO<sub>2</sub>-TPD profiles of the reduced Ni/Ce, Ni/Sm-Ce, Ni/Pr-Ce and Ni/Mg-Ce catalysts.

### 3.4. Ni species reducibility (TPR-H<sub>2</sub>)

H<sub>2</sub>-TPR experiments (Fig. 5) were performed in order to investigate the reducibility of the catalytic samples and to study the interaction strength of Ni particles with the support surfaces. It is noted that CeO<sub>2</sub> does not present reduction peaks at temperatures lower than 500 °C [71]. As can be seen in Fig. 5, Sm<sup>3+</sup>, Pr<sup>3+</sup> and Mg<sup>2+</sup> doping caused a modification in the H<sub>2</sub>-TPR profiles of the modified catalytic samples as the hydrogen consumption peaks, in terms of position, shape and intensity, showing differences, which indicate that the reducibility of the catalytic samples is affected by the dopant addition into CeO<sub>2</sub> lattice.

Specifically, three hydrogen consumption peaks, denoted as region I, II and III are presented for all catalytic samples. The first reduction peak (region I) located at low temperature ( $\approx 200$  °C) can be attributed to the reduction of highly dispersive NiO species on the surface of the prepared supports [59]. Between 225–425 °C a significant hydrogen consumption peak (region II) can be observed, which can be ascribed to the reduction of dispersed NiO species interacting with (but not chemically bound to) the support. The hydrogen consumption peak (region III) detected at higher temperature ( $\approx 420$  °C) probably corresponds to the formation of solid solution between metal and support [72]. Moreover, the H<sub>2</sub>-TPR profiles show that the reduction of dispersed NiO species (region I), as well as, NiO species in interaction with the Ce<sup>4+</sup> (originating from the

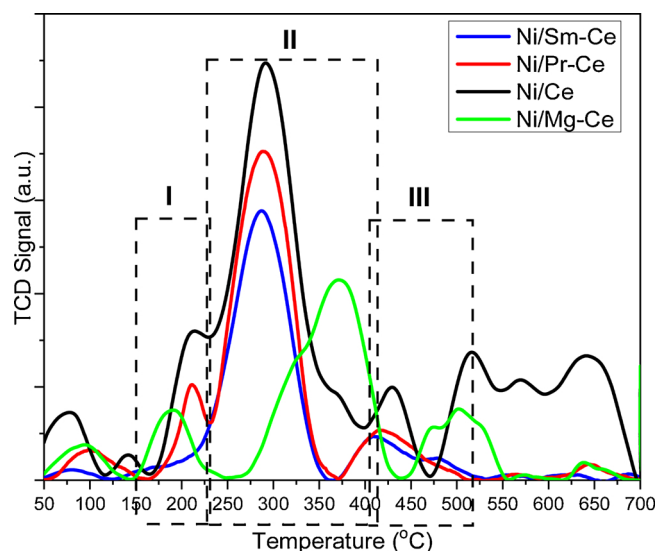


Fig. 5. H<sub>2</sub>-TPR profiles of the Ni/Ce, Ni/Sm-Ce, Ni/Pr-Ce and Ni/Mg-Ce catalysts.

lattice) (early temperatures of region III), occurs at a lower temperature for the Ni/Sm-Ce and Ni/Pr-Ce catalysts when compared with the unmodified catalyst. The temperature regimes for the different NiO species reduction (free/dispersed NiO, NiO in surface interaction with the lattice and NiO in strong interaction with the lattice) are in agreement with published data [73]. According to other published research, the highly dispersed NiO particles, depending on their size as well, are reduced in the 250–350 °C range, whereas at 400–500 °C are the NiO clusters in interaction with ceria [74,75]. The reduction peaks in the higher temperature region (485–675 °C) are a bit more complicated. On the one hand, they could be partially attributed to the NiO species having strong interaction with the carrier; on the other hand, they could be also assigned to the reduction of surface/subsurface of the ceria based support.

According to the literature, the addition of lanthanides into the lattice of CeO<sub>2</sub> improves the NiO oxygen lability (decreases the reduction temperature) meaning that the shift observed depends on the lanthanide: Sm = Pr < Ce [76]. However, the contribution of different sized nickel species, activated at different reduction temperature cannot be dismissed [77]. The hydrogen consumption peak at high reduction temperatures can be attributed to the reduction of bulk CeO<sub>2</sub> (Ce<sup>4+</sup> to Ce<sup>3+</sup>) particles [78]. Finally, as can be seen from the H<sub>2</sub>-TPR profile of Ni/Mg-Ce catalyst, the addition of Mg<sup>2+</sup> into the lattice of CeO<sub>2</sub> affect the reduction temperatures of nickel species II and III. According to the literature, the reduction at higher temperature is probably due to the greater electronegativity of Mg (1.31), which is higher than that of Ce (1.12), Sm (1.17) and Pr (1.13) leading to stronger electron-withdrawing property of Mg making more difficult the reduction of the NiO species [79].

### 3.5. H<sub>2</sub> chemisorption

The strength of H<sub>2</sub> interaction with the Ni centres, as well as, the amount of chemisorbed H<sub>2</sub> (a good estimate of the metal dispersion and mean particle size) were determined via H<sub>2</sub>-TPD experiments performed on the reduced Ni/Ce, Ni/Sm-Ce, Ni/Pr-Ce and Ni/Mg-Ce catalysts. The H<sub>2</sub>-TPD profiles (Figure S1) show a main peak of desorbed H<sub>2</sub> situated at temperature lower than 450 °C for all samples. According to the literature [80,81], this peak is generally attributed to H<sub>2</sub> desorbed from the active metal sites, while, H<sub>2</sub> desorption peaks at temperatures higher than 450 °C may come from H<sub>2</sub> located in the subsurface layers, H<sub>2</sub> spillover and/or reoxidation of Ni by water inherent on the sample after reduction [80,82]. Moreover, as can be seen from Table 2, the amount of H<sub>2</sub> desorbed from the catalyst surface did not vary greatly between the

**Table 2**  
H<sub>2</sub> desorption, Ni dispersion and mean particle.

Catalyst	H <sub>2</sub> , μmol/g	D <sub>Ni</sub> , %	d <sub>Ni</sub> , nm	d <sub>(Ni)</sub> , nm <sup>1</sup>
Ni/Ce	2668	8.5	11.4	4.4 ± 1.5
Ni/Sm-Ce	2488	8.0	12.2	3.6 ± 1.3
Ni/Pr-Ce	2436	7.8	12.4	3.4 ± 1.0
Ni/Mg-Ce	2840	9.1	10.7	3.7 ± 1.2

Note: <sup>1</sup>Based on TEM.

catalytic samples and thus, Ni dispersion (D<sub>Ni</sub>, %) and the mean Ni particle size (d<sub>Ni</sub>) were also quite similar. In particular, the mean Ni particle size was found to be 11.4, 12.2, 12.4 and 10.7 nm for the Ni/Ce, Ni/Sm-Ce, Ni/Pr-Ce and Ni/Mg-Ce catalysts, respectively. These values are somewhat different than those obtained via electron microscopy, but the difference can be understood on the basis of the techniques used. For example, the chemisorption technique is linked with spherical shapes, which have the lowest surface area (S) per volume (V) ratio of all the geometric shapes [83]. The detrimental importance of particle shape in the investigation of the chemical/physical particle's characteristics is well documented in the literature [84,85]; however, the potential error in the calculation of the particle size by chemisorption does not affect the adsorption strength of the probe molecules (such as hydrogen) to the different exposed facets [86]. The adsorption of probe molecule chemisorption is also important. There are reports in the literature where they demonstrate the need of even cryogenic conditions, to achieve saturation of the metal surfaces with the probe molecule, for a variety of geometries, shapes and sizes [87]. However, it is noted that both techniques show that the catalytic materials did not exhibit great differences in terms of Ni particle size.

### 3.6. Surface analysis (XPS)

Firstly, it should be noted that the XPS analysis was undertaken on the reduced catalysts, ex-situ following atmospheric exposure. For the Ni/Ce, Ni/Pr-Ce, Ni/Sm-Ce and Ni/Mg-Ce catalysts, the XPS survey scan and following core level peaks were recorded: Ni 2p, Ce 3d, Pr 3d, Sm 3d, Mg 1s, O 1s and C 1s. The Ni 2p, Ce 3d and O 1s peaks for all catalysts are given in Figs. 6 (a), (b) and (c) respectively. The Pr 3d, Sm 3d and Mg 1s peaks for the doped catalysts are presented in Figs. 6 (d), (e) and (f) respectively. A small concentration of Na was observed on all samples as a contaminant, which can be seen in Fig. 6 (d).

Considering first the Ni 2p peaks, for the pure CeO<sub>2</sub> catalyst and the doped catalysts, the general Ni 2p peakshape is similar, with their being a broad Ni 2p<sub>3/2</sub> peak located at 855.8 ± 0.2 eV and a distinct shoulder at 853.0 ± 0.2 eV. The low binding energy peak corresponds to Ni metal (Ni<sup>0</sup>) species, whilst the peak at 855.8 eV represents predominantly Ni(OH)<sub>2</sub>[88]. Even though there is no clear shoulder apparent between the 853.0 eV and 855.8 eV peaks in these spectra, the broadened nature of the lower binding energy edge of the 855.8 eV peak indicates the presence of a further peak in this region. This is further supported by a simple peak fit employing just the 853.0 and 855.8 eV components, which shows that there is a definitely a further peak located in this middle energy region. As seen in ref [89]. and other work where we have investigated Ni on metal oxide support based catalytic systems, e.g. [89], this peak most probably corresponds to some NiO (around 854.5 eV) being present on all catalysts. It should be noted that the complex peakshapes (including multiplet splitting, plasmon loss and satellite features) of the many different Ni oxide/hydroxide species [90] which could be present on the surface precludes a reliable peak fit being presented. Again, from a simple peak fit of the Ni<sub>me</sub> and Ni<sub>ox</sub> peaks at 853.0 and 855.8 eV respectively, it is possible to estimate the Ni<sub>me</sub>/Ni<sub>ox</sub> peak area ratio, the results of which are given in Table 3. It can be seen that there is a stronger Ni<sub>me</sub> intensity for the Ni/Pr-Ce and Ni/Sm-Ce compared to the Ni/Mg-Ce and Ni/Ce catalysts,

suggesting that the former catalysts exhibit more highly reduced surfaces than the latter catalysts.

The Ce 3d peaks presented in Fig. 6 (b) are also complex and the numerous peaks are labelled in accordance with the nomenclature used in previous XPS work on cerium oxide [91–93]. The peaks are labelled as v and u, corresponding to Ce 3d<sub>5/2</sub> and Ce 3d<sub>3/2</sub>, transitions respectively. The main peaks are v, v', v'', u, u', u'' corresponding to Ce<sup>4+</sup> species, with peaks labelled as v' and u' corresponding to Ce<sup>3+</sup> species. The Ce 3d spectra show that the cerium oxide is wholly or predominantly a Ce<sup>4+</sup> based oxide, in agreement with the XRD and Raman data.

Examining now the XPS concentrations and spectra of the dopant species. Table 3 gives the XPS determined elemental concentrations in the doped catalysts, showing Pr, Sm and Mg to be present at concentrations of 3.4, 2.6 and 2.5 at.% respectively.

The Pr 3d peaks are given in Fig. 6 (d). This Pr 3d spectral peakshape is in excellent agreement with the Pr 3d spectrum for Pr<sub>2</sub>O<sub>3</sub> presented by Ogasawara et al. [94], and a sample containing 95% Pr<sup>3+</sup> given by Mekki et al. [95]. The 3d<sub>5/2</sub> peak is observed at a binding energy of 933.3 eV, in excellent agreement with that given in [95] and [96]. The 3d<sub>5/2</sub> and 3d<sub>3/2</sub> peakshave associated satellite features at lower binding energies and the 3d<sub>3/2</sub> peak has an additional small peak at higher binding energy, attributed by Ogasawara et al. to a multiplet effect [94]. PrO<sub>2</sub> (Pr<sup>4+</sup>) has a similar peakshape to Pr<sub>2</sub>O<sub>3</sub>, but there are small differences in the fine structure and the 3d<sub>5/2</sub> peak position is given as 935.5 eV [95]. Thus, the Pr substitutionally incorporated in CeO<sub>2</sub> in the Ni/Ce-Pr catalyst is present as Pr<sup>3+</sup>.

The Sm 3d<sub>5/2</sub> peak for the Ni/Ce-Sm catalyst is shown in Fig. 6 (e). An XPS spectrum from a commercial Sm<sub>2</sub>O<sub>3</sub> powder was also recorded. This sample was considered as a good reference sample as it exhibited a stoichiometry of Sm<sub>2</sub>O<sub>2.9</sub> and a small concentration of carbonaceous contaminant species. The Sm 3d peaks for the Ni/Ce-Sm catalyst shown in Fig. 6 (e) exhibit the same peak shape as the Sm<sub>2</sub>O<sub>2.9</sub> powder and the binding energy of the Sm 3d<sub>5/2</sub> peak and 3d peakshape is in good agreement with other reports for Sm<sub>2</sub>O<sub>3</sub>[97,98]. Thus, similar to Pr in the Ni/Ce-Pr catalyst, Sm also exists in a 3+ oxidation state in the Ni/Ce-Sm catalyst.

The XPS Mg 1s peak is shown in Fig. 6 (f). The Mg 1s peak exhibits a binding energy of 1304.2 eV, which compares very well with other values for MgO [99]. This is consistent with the XRD results in Fig. 2, which indicated the formation of MgO as a separate phase to CeO<sub>2</sub>, rather than solid solution incorporation of Mg into the CeO<sub>2</sub> structure.

### 3.7. Electron microscopy analysis

Fig. 7 presents the HAADF-STEM images, EDS spectra and particle size distribution histograms obtained for the reduced Ni/Ce (Fig. 7a), Ni/Sm-Ce (Fig. 7b), Ni/Pr-Ce (Fig. 7c) and Ni/Mg-Ce (Fig. 7d) catalysts. HAADF-STEM images have Z-contrast, where heavy atoms have high brightness. As can be seen in Fig. 7, the larger particle sizes (> 20 nm) depicted in the HAADF-STEM images can be assigned to spongy porous uniform nanospheres of CeO<sub>2</sub> structures [100,101]. Moreover, the resulting EDS mapping patterns confirms the presence of Ni and Ce on all samples and Sm and/or Pr on the corresponding promoted catalysts as expected. It is noted that the identification of Cu on the EDS spectra for all samples is due to the TEM grid-support used in the analysis. From the particle size distribution histograms, the mean nickel particle size followed the order Ni/Ce (4.4 ± 1.5 nm) > Ni/Mg-Ce (3.7 ± 1.2 nm) > Ni/Sm-Ce (3.6 ± 1.2 nm) > Ni/Pr-Ce (3.4 ± 1.0 nm). Thus, it can be concluded that the addition of dopants (Mg<sup>2+</sup>, Sm<sup>3+</sup> and Pr<sup>3+</sup>) helped obtain slightly smaller Ni nanoparticles.

### 3.8. Catalytic performance

The reproducibility of the experimental results was tested by carrying out a number of repeat experiments (at least three times). From these experiments, 95% confidence intervals for the mean value were calculated and it was found that the individual experimental values lay

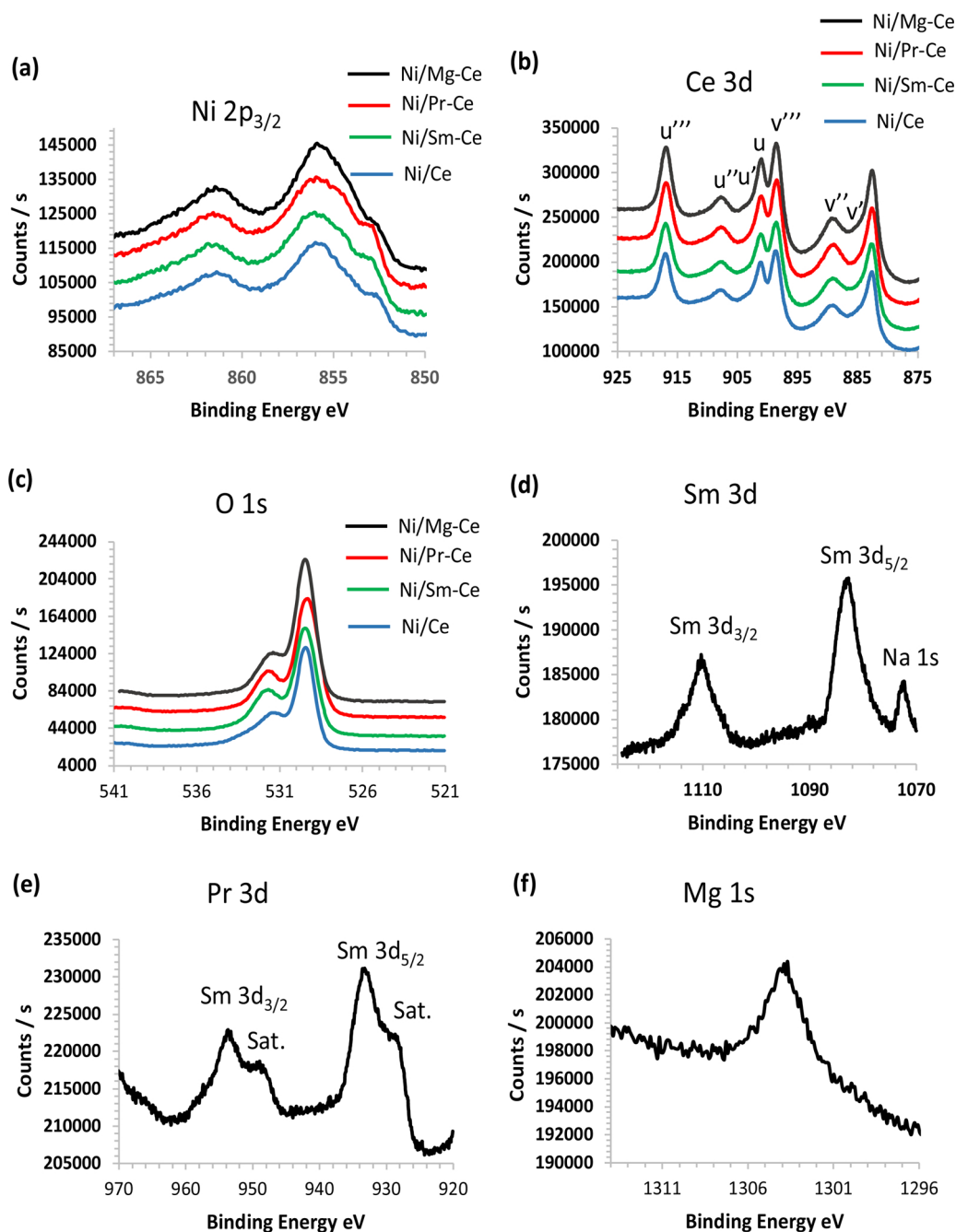


Fig. 6. XPS core level spectra (reduced catalysts) from Ni on pure CeO<sub>2</sub> and Pr/Sm/Mg doped CeO<sub>2</sub> supports.

(a) Ni 2p, (b) Ce 3d, (c) O 1s, (d) Sm 3d, (e) Pr 3d, (f) Mg 1s.

Table 3

XPS determined elemental concentrations and Ni<sub>me</sub>/Ni<sub>ox</sub> peak area ratios for the reduced Ni/Ce, Ni/Sm-Ce, Ni/Pr-Ce, Ni/Mg-Ce catalysts.

Catalyst	Ni	Ce	O	Sm	Pr	Mg	Peak area ratio (Ni <sub>me</sub> /Ni <sub>ox</sub> )
Ni/Ce	12.8	17.7	69.5				0.25
Ni/Sm-Ce	12.8	17.1	67.7	2.6			0.28
Ni/Pr-Ce	12.9	16.7	67.0		3.4		0.28
Ni/Mg-Ce	12.7	18.6	66.2			2.5	0.22

well within the corresponding confidence intervals showing a very good reproducibility of the repeated experiments. The only reaction products detected were CH<sub>4</sub> and CO and carbon balance was found to close well, with deviations of less than ~3%.

Fig. 8(a–c) shows the influence of reaction temperature in the range of 200–500 °C to CO<sub>2</sub> conversion (X<sub>CO2</sub>, %), CH<sub>4</sub> and CO selectivities (S<sub>CH4</sub> and S<sub>CO</sub>, %) as well as the CH<sub>4</sub> yield (Y<sub>CH4</sub>, %) of the catalysts tested herein.

As can be seen, the X<sub>CO2</sub> increases as the temperature rises from 250 to 400 °C for all catalytic samples. The largest differences in activity between the catalysts are recorded at 350 °C where X<sub>CO2</sub> takes the value 39.4% (Ni/Ce), 44.9% (Ni/Sm-Ce), 54.5% (Ni/Pr-Ce) and 43.2% (Ni/Mg-Ce) (Table 4). Thus, from the results presented herein, the un-promoted catalytic sample is the least active and the Ni catalyst supported on Pr-Ce appears to be more active in terms of X<sub>CO2</sub> and Y<sub>CH4</sub> in comparison with the other promoted catalytic samples. In particular, for the X<sub>CO2</sub> values presented above, compared to pure Ni/Ce catalyst, Ni/Pr-Ce catalytic sample shows an increase of 38%. Moreover, the Ni/Sm-Ce

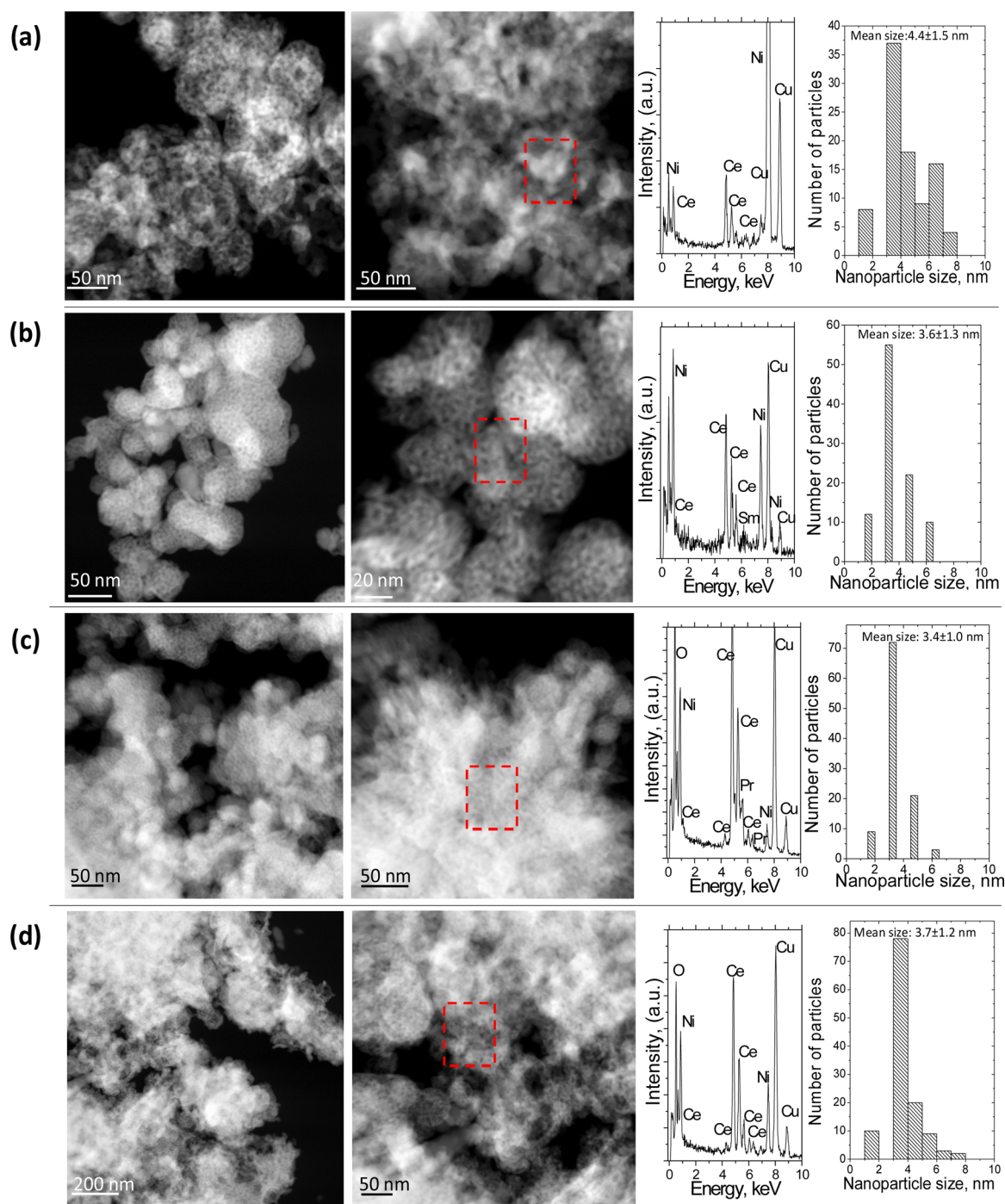


**Fig. 7.** HAADF-STEM images with Z-contrast (heavy atoms have high brightness, EDS spectrum of red-dashed area marked and particle size distribution histogram of the a) Ni/Ce, b) Ni/Sm-Ce, c) Ni/Pr-Ce and d) Ni/Mg-Ce reduced catalysts. (For interpretation of the references to colour in this figure legend, the reader is referred to the web version of this article).

and Ni/Mg-Ce catalysts appear quite similar in terms of their total activity. In addition, it is worth noting that the  $X_{CO_2}$  decreases at temperatures higher than 400 °C for all samples. This is due to the fact that the exothermic  $CO_2$  methanation reaction is not thermodynamically favoured at high temperatures; specifically, at  $T > 600$  °C the Gibbs free energy change of the methanation reaction (Eq. 1) takes positive values. An additional factor could be the agglomeration of nickel nanoparticles at the high operating temperature (decreasing the Ni active sites) [102]. Further, as shown in Fig. 8b, for all catalytic samples  $S_{CH_4}$  is close to 100% up to 400 °C, and then, decreases slightly, while  $S_{CO}$  increases with temperature, probably due to (i) the exothermic character of the  $CO_2$  methanation reaction, and (ii) the endothermic

character of the reverse water gas shift reaction [74]. Comparing the catalytic performance in terms of  $S_{CH_4}$  and  $S_{CO}$ , it seems that Ni/Pr-Ce sample has the highest  $S_{CH_4}$  and the lowest  $S_{CO}$  for the whole temperature range. This according to the literature can be mostly due to the different intermediate species, as those tracked by FTIR spectroscopy, formed under reaction conditions in the case of Ni/Pr-Ce catalysts, i.e., carboxylate and carbonate are possible species, with the latter favouring the  $CO_2$  reduction to CO (unfavourable product) [103,104].

The intrinsic activity of the above Ni based catalysts has been investigated under differential reaction conditions and the results obtained are presented in Figure S2. In particular, the turnover frequencies (TOFs) were calculated based on  $CO_2$  conversion over the

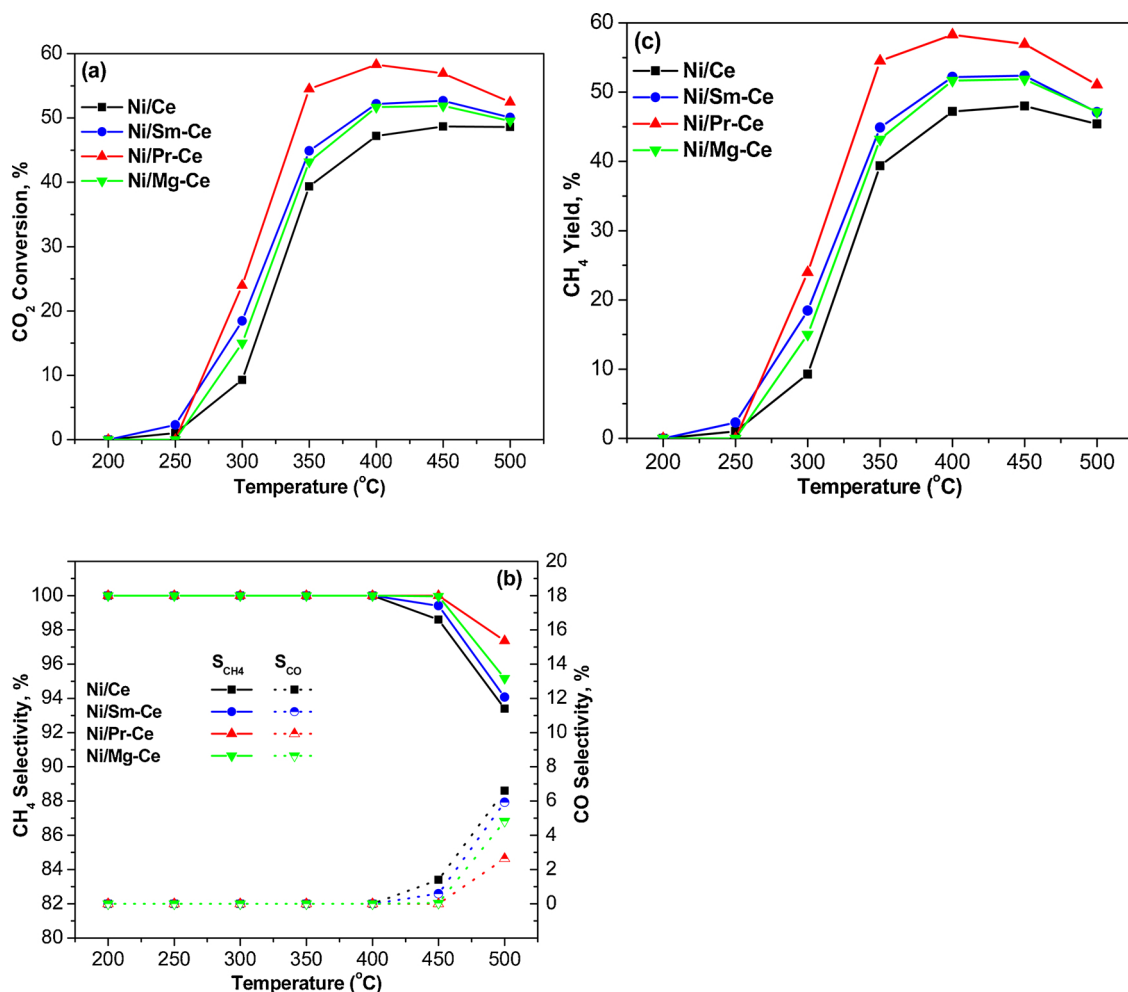


Fig. 8. Catalytic performance for Ni/Ce, Ni/Sm-Ce, Ni/Pr-Ce and Ni/Mg-Ce as a function of reaction temperature: (a) CO<sub>2</sub> Conversion, (b) CH<sub>4</sub> and CO selectivity and (c) CH<sub>4</sub> Yield; Reaction conditions: Experimental Protocol #1.

**Table 4**  
Comparison of catalysts activity at 300 and in parenthesis, at 350 °C.

Catalyst	Conversion CO <sub>2</sub> (%)	Yield CH <sub>4</sub> (%)	Selectivity CH <sub>4</sub> (%)
Ni/Ce	9.3 (39.4)	9.3 (39.4)	100 (100)
Ni/Sm-Ce	18.5 (44.9)	18.5 (44.9)	100 (100)
Ni/Pr-Ce	24.0 (54.5)	24.0 (54.5)	100 (100)
Ni/Mg-Ce	15.0 (43.2)	15.0 (43.2)	100 (100)

desorbed H<sub>2</sub>, in order to investigate the intrinsic reactivity per surface of Ni site. As can be observed, the TOF values follow the order Ni/Pr-Ce >> Ni/Mg-Ce > Ni/Sm-Ce > Ni/Ce, thus the Pr-promoted sample appears more active for the whole temperature range.

### 3.9. Catalytic stability

The catalytic stability tests were performed at constant reaction temperature of 400 °C under experimental protocol #2 for 20 h; the aim of these experiments were: (a) the investigation of possible carbon formation on the catalyst surface via CO disproportionation ( $2\text{CO} \rightleftharpoons \text{C} + \text{CO}_2$ ) or via incomplete CO reduction reaction ( $\text{CO} + \text{H}_2 \rightleftharpoons \text{C} + \text{H}_2\text{O}$ ) and its effect on catalytic stability, and (b) the investigation of the extent of nickel nanoparticles sintering [105]. As shown in Fig. 9(a-c), the catalytic activity followed the order: Ni/Pr-Ce >> Ni/Mg-Ce > Ni/Sm-Ce = Ni/Ce, which indicates that performance (as a function of time) depends on the support nature, as well as, to the promoting effect

of dopants (Mg<sup>2+</sup>, Sm<sup>3+</sup> and Pr<sup>3+</sup>). The remarkable performance of the Ni/Pr-Ce catalyst in terms of CO<sub>2</sub> conversion during the time on stream experiments, can be attributed to the interaction/synergism between Ni and praseodymium oxide that leads to the formation of stable and high capacity hydrogen adsorption sites [106,107] and the fact that the addition of f-block element can influence the acid-base properties enhancing the activity and stability of the catalysts [12,108,109]. Regarding the CH<sub>4</sub> selectivity and yield, it is clear from Fig. 9b that the doped catalysts show highly stable CH<sub>4</sub> values for the duration of the 20 h time on stream experiments, which suggests that the deactivation of the catalytic samples has been successfully prevented.

In order to further investigate catalytic stability, additional time on stream experiments were carried out, also at 400 °C (Fig. 10), at more severe conditions (increased concentration of CO<sub>2</sub>); these experiments were carried out for 7 h. As depicted in Fig. 10a-c, the catalytic activity in terms of CO<sub>2</sub> conversion, CH<sub>4</sub> and CO selectivity and CH<sub>4</sub> yield is stable and almost similar for all samples. However, it is worth mentioning that comparing the catalytic performance between experimental protocols #2 and #3, a decrease up to 40% of the catalytic performance in terms of CO<sub>2</sub> conversion and CH<sub>4</sub> yield can be observed. This finding can be assigned to the lower H<sub>2</sub> concentration in the gas stream feedstock, leading to less dissociated H<sub>2</sub> into H on the active sites of the catalyst, suppressing the CO<sub>2</sub> methanation reaction.

According to the literature [110,111], during the CO<sub>2</sub> methanation process, gaseous H<sub>2</sub> is usually activated and dissociated over the metallic Ni nanoparticles. Garbarino et al. [112] showed that the selectivity of CH<sub>4</sub> is related to the Ni particle size and specifically, that

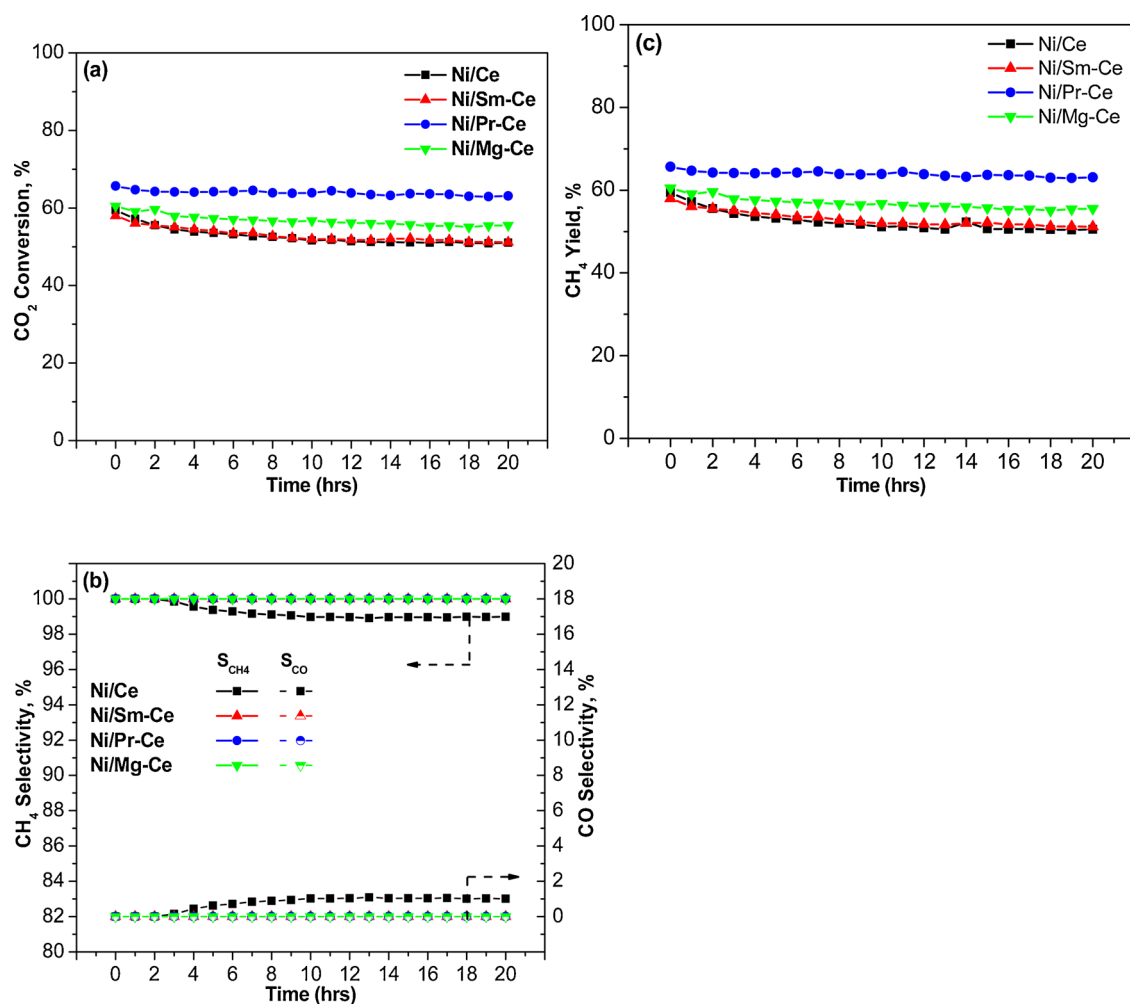


Fig. 9. Stability tests for Ni/Ce, Ni/Sm-Ce, Ni/Pr-Ce and Ni/Mg-Ce as a function of reaction time: (a) CO<sub>2</sub> Conversion, (b) CH<sub>4</sub> and CO selectivity and (c) CH<sub>4</sub> Yield; Reaction conditions: Experimental Protocol #2.

smaller Ni particles are very selective to CH<sub>4</sub> without the formation of gaseous CO. Thus, for the catalysts tested herein, the possible thermal sintering of the metallic nanoparticles would seriously affect their activation by suppressing the dissociation of the H<sub>2</sub> into H and the following hydrogenation of the reaction intermediates, leading to decreased CH<sub>4</sub> selectivity, due to the low capacity for hydrogen absorption sites [110].

### 3.10. Characterization of the spent catalysts

The morphology of the spent catalysts tested under experimental protocol #2 and #3 was examined using TEM (Figs. 11&12), in order to delineate the extent of metal particle sintering and carbon deposition, the main reasons for the deactivation of Ni based catalysts. From the images obtained, and for both experimental protocols, carbon deposits are absent on all samples, which may indicate that the surface coke formed a very thin layer not detectable at the working magnification. As has been previously reported [26,113], the use of lanthanides and basic character ions as promoters can suppress the formation of coke, an obvious advantage for catalytic stability.

However, the histograms of the spent catalysts (Fig. 12) reveal that the sintering of the metallic Ni particles was quite extensive. Specifically, after 20 h time-on-stream (experimental protocol #2) the mean diameter of nickel particles increased substantially from their initial values, following the order Ni/Ce (35.2 ± 18.1 nm) > Ni/Sm-Ce (29.5 ± 17.6 nm) > Ni/Pr-Ce (19.5 ± 6.7 nm) > Ni/Mg-Ce (17.5 ± 9.8 nm). Similarly, particle size

followed the order Ni/Ce (18.5 ± 18.3 nm) > Ni/Sm-Ce (15.2 ± 7.8 nm) > Ni/Pr-Ce (13.9 ± 6.5 nm) > Ni/Mg-Ce (13.7 ± 5.3 nm) for the spent catalyst tested under experimental protocol #3.

### 3.11. Correlation between physico-chemical properties and catalytic performance

As is well understood, the intrinsic behavior of any catalytic system is directly related to a complex set of interwoven factors, which include the dispersion of active phase, the extent of metal support interactions, its acid/basic properties and its oxygen vacancies availability. According to the literature [108,110], the *synergism between Ni and promoter oxides* could lead to the genesis of a large quantity of stable and high capacity hydrogen adsorption sites residing either on the metal or on the metal-support interface. Moreover, the addition of lanthanides and/or basic ions can alter the surface acidity/basicity of catalysts, which can also be of benefit to catalytic activity and stability. Specifically, for the methanation reaction, gaseous CO<sub>2</sub> is adsorbed and dissociated on medium basic sites forming covalent carbonates, hydrogen carbonates and bidentate carbonates, and then reacts with dissociated H atoms on Ni<sup>0</sup> particles to form formates and finally to produce methane (one possible route; with carboxylates and formates routes being alternative ones) [114]. This means that improved CO<sub>2</sub> adsorption on basic sites can increase activity at low reaction temperatures [115]. As an example, Le et al. [116] reported that the addition of Na with different content (0.1 and 1 wt.%) as promoter on Ni/CeO<sub>2</sub>

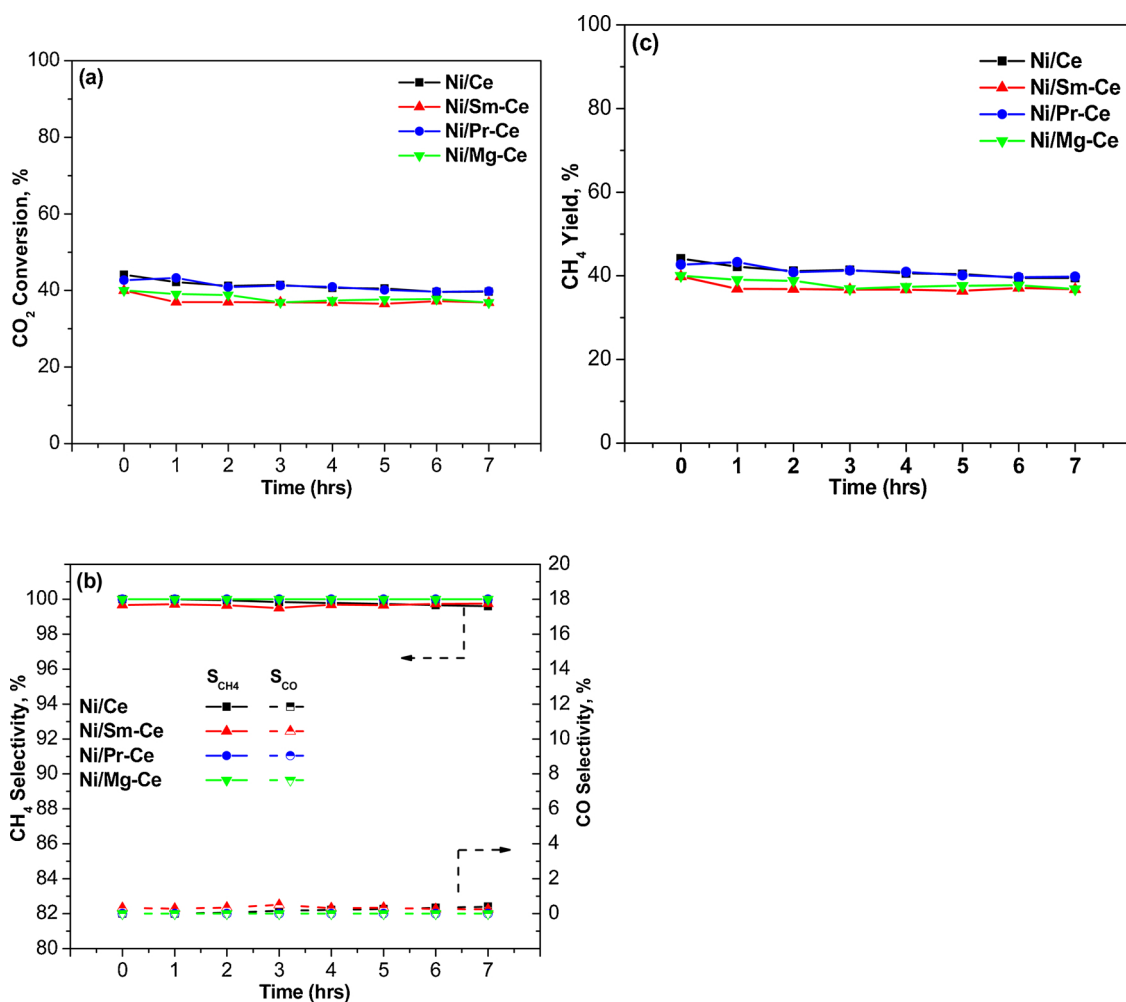


Fig. 10. Stability tests for Ni/Ce, Ni/Sm-Ce, Ni/Pr-Ce and Ni/Mg-Ce as a function of reaction time: (a) CO<sub>2</sub> Conversion, (b) CH<sub>4</sub> and CO selectivity and (c) CH<sub>4</sub> Yield; Reaction conditions: Experimental Protocol #3.

catalyst decreased the basicity (CO<sub>2</sub> chemisorbed) and the Ni dispersion of the catalytic sample, and as a result, led to lower activity in terms of the CO<sub>2</sub> methanation reaction. Moreover, the effect of sodium on Ni/CeO<sub>2</sub> was investigated for the water gas shift reaction [117] and the author showed that the Na<sup>+</sup> displaced Ce<sup>4+</sup> in the CeO<sub>2</sub> lattice, generating oxygen vacancies and increased oxygen mobility. On the other hand, Li et al. [68] observed that the simultaneous presence of La and Ce reinforced the basicity and thus, the adsorption sites on the catalyst surface, leading to the improvement of the methanation reaction at low temperatures. Wierzbicki et al. [118], examining La-promoted and unpromoted catalytic samples, showed that the activity and the number of basic sites of medium strength are almost linearly correlated. In fact, one may find a plethora of published studies that show that the introduction of rare earths (Sm, Ce, Y) and alkaline-earth metals (Mg, Ca, Sr, Ba) on supporting materials substantially increases the catalytic activity in the CO<sub>2</sub> methanation reaction as a result of the increased number of medium strength basic sites [12,119–124].

Apart from basicity, the *dispersion of active phase* is another crucial factor that influences activity. Sun et al. [119] argued that the decrease of nickel particle size led to increased medium strength basic sites and stronger metal-support interactions, contributing to enhanced catalytic performance. Ahmad et al. [125] investigating the effect of the addition of lanthanides (La, Ce, Pr, Eu and Gd) on 12%Ni/Al<sub>2</sub>O<sub>3</sub> catalyst, showed that the improvement of the catalytic performance was due to the highest dispersion of active H species on the promoted catalysts. Bian et al. [126] studied the CO<sub>2</sub> methanation activity at low temperatures, on a plasma-prepared Ni based catalyst, and proved that the

addition of CeO<sub>2</sub> reinforced the Ni dispersion, leading to increased catalytic activity.

Additionally, it has been shown that the existence of *oxygen vacancies* in catalytic systems plays a key role in improving the CO<sub>2</sub> methanation activity [127]. Oxygen vacancies participate in CO<sub>2</sub> methanation reaction by storing and releasing oxygen and/or improving the dispersion of hydrogen adsorption sites [128]. Moreover, it has been observed that oxygen vacancies cause the formation of (i) surface carbon species, an intermediate species to form methane, and (ii) interact with CO<sub>2</sub> molecules, contributing to the change of the O–C–O angle, weakening of the C=O bonds and finally the cleavage of the C=O bond. Specifically, Takano et al. [127,129] studied the effect of heat treatment on the performance of zirconia based modified catalysts in CO<sub>2</sub> methanation and reported that the Ni/(Zr-Sm) catalyst exhibited higher catalytic performance than Ni-Zr. The authors showed that the Sm<sup>3+</sup> caused the substitution of Zr<sup>4+</sup> generating oxygen vacancies, which interact with the oxygen in CO<sub>2</sub> molecules, weakening the C=O bond and thus, strengthening the CO<sub>2</sub> hydrogenation towards CH<sub>4</sub>. Ashok et al. [130] suggested that the incorporation of Ni<sup>2+</sup> into the lattice of Ce<sub>x</sub>Zr<sub>1-x</sub>O<sub>2</sub> support generates oxygen vacancies, reinforcing adsorption of oxygenate species. Alkhoori et al. [131] showed, through experimental and theoretical studies, that doping ceria with Sm<sup>3+</sup> and Cu<sup>2+</sup> lowers significantly the energy of oxygen vacant sites formation through the creation of new energy states that facilitate the hosting of the electron pair left behind during the oxygen departure from the structure. At the same time the dopant type and valence lead to the formation of different oxygen vacancies configurations/clusters located on the surface and

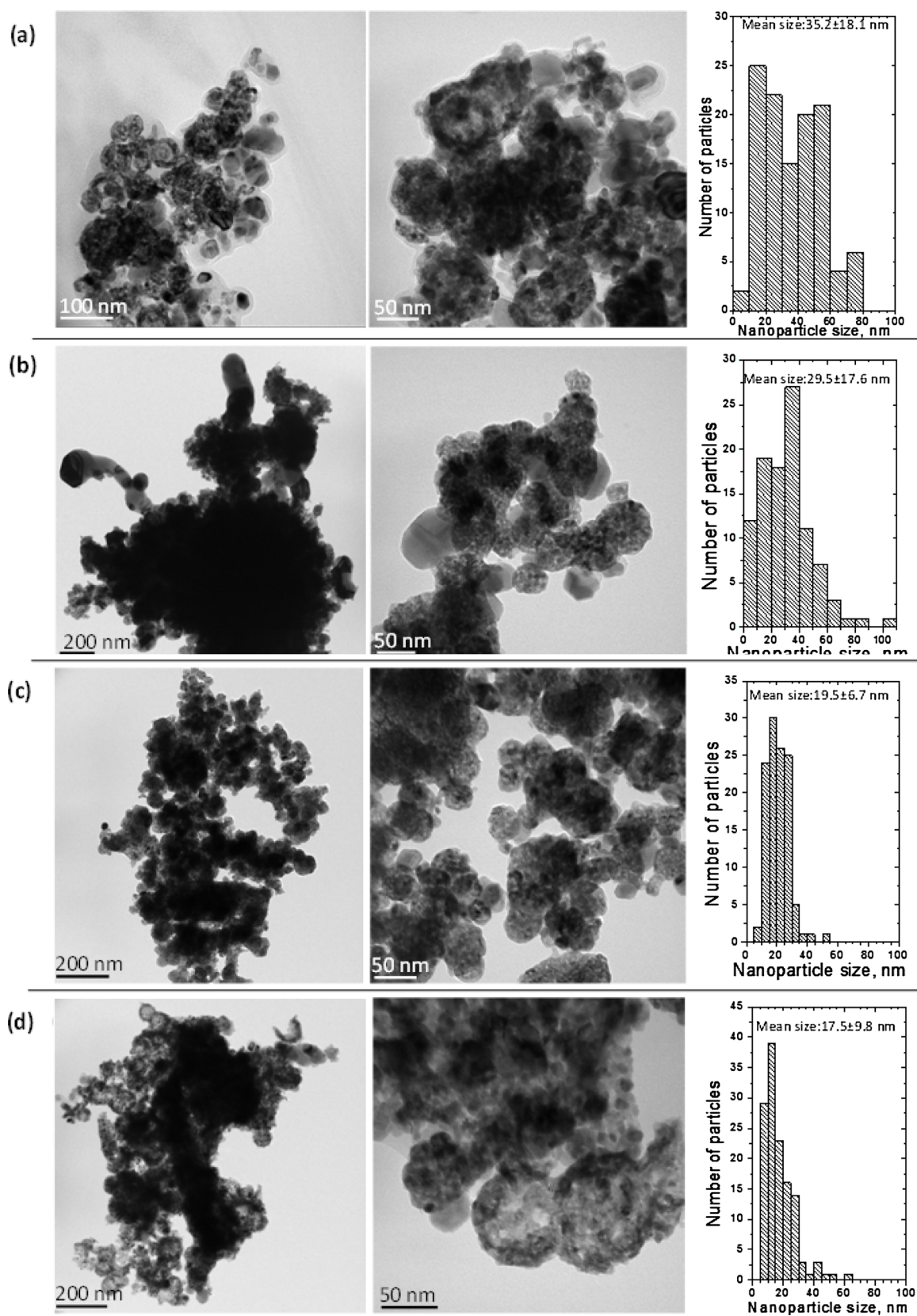
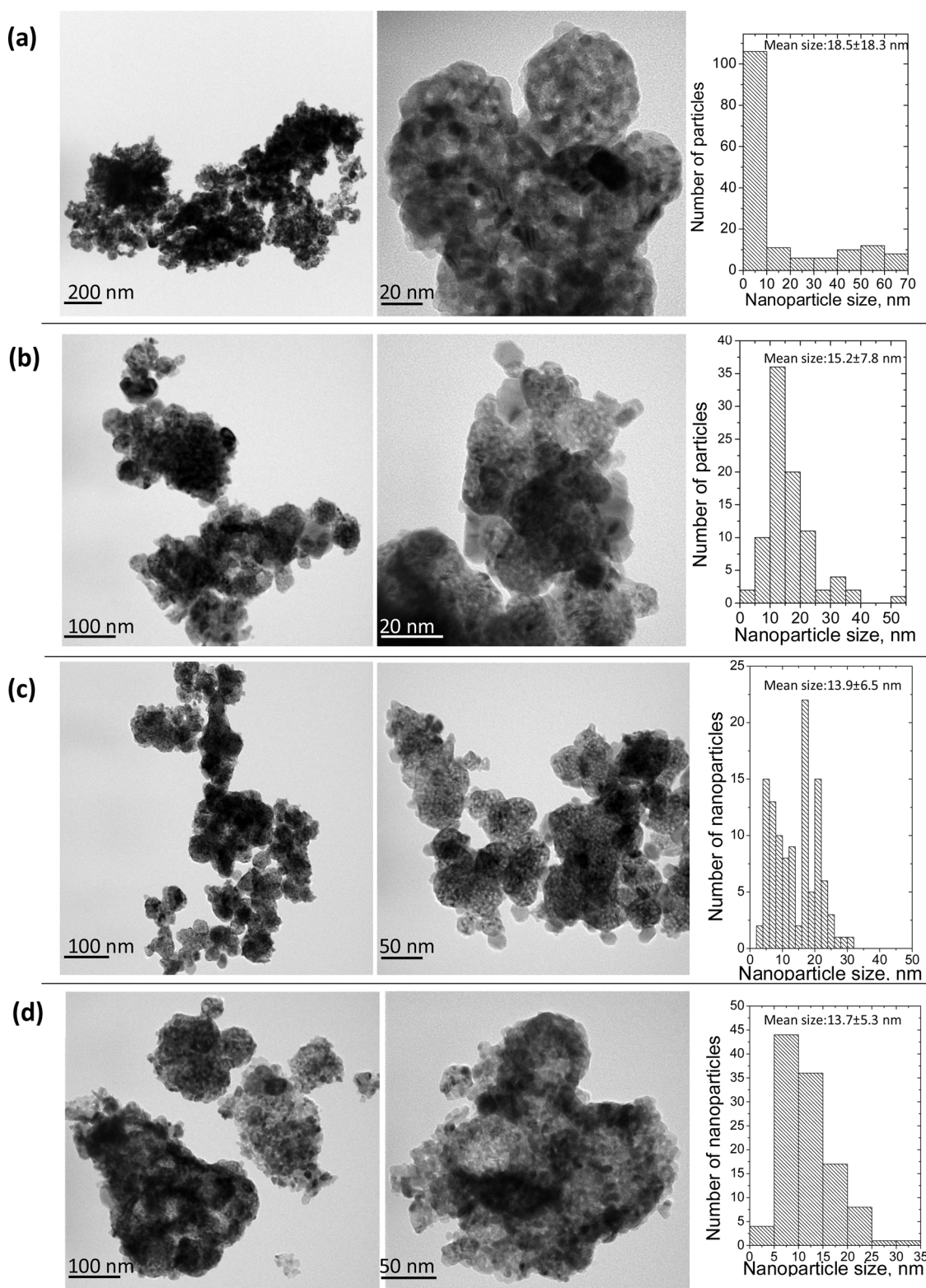


Fig. 11. TEM images and particle size distribution histogram of: a) Ni/Ce, b) Ni/Sm-Ce, c) Ni/Pr-Ce and d) Ni/Mg-Ce [Results obtained for samples tested under experimental protocol #2].

subsurface. Liang et al. [51] showed that modification with Sr species forms oxygen vacancies leading to Lewis basic positions, improving the CO<sub>2</sub> methanation reaction at low reaction temperature.

From the results presented herein (Fig. 8), the addition of modifiers (Sm<sup>3+</sup>, Pr<sup>3+</sup> and Mg<sup>2+</sup>) led to the formation of lower Ni crystalline sizes (higher dispersion) however, as the difference between the samples is not



**Fig. 12.** TEM images and particle size distribution histogram of: a) Ni/Ce, b) Ni/Sm-Ce, c) Ni/Pr-Ce and d) Ni/Mg-Ce [Results obtained for samples tested under experimental protocol #3].

very large (e.g.,  $4.4 \pm 1.5$  nm for the Ni/Ce catalyst as opposed to  $3.4 \pm 1.0$  nm for the Ni/Pr-Ce, based on TEM measurements) it can be argued that the enhanced catalytic performance at low reaction temperature was mainly a result of the beneficial effects of abundance in oxygen vacancies, increased basicity and stronger metal-support interactions. In particular, based on the XRD, Raman and XPS analysis of the

Ni/Sm-Ce and Ni/Pr-Ce, it can be seen that the Sm and Pr incorporated into  $\text{CeO}_2$  lattice as  $\text{Sm}^{3+}$  and  $\text{Pr}^{3+}$ , respectively, creating oxygen vacancies; this in turn proved beneficial for the activation of the  $\text{CO}_2$  molecule in the  $\text{CO}_2$  methanation reaction at low reaction temperature.

It has to be mentioned at this point that *not only the population but also the location of the oxygen vacant sites* is very important. The Raman

studies, presented earlier, showed that the  $O_v/F_{2g}$  ratio (descriptor of the  $O_v$  population) follows the order: Ni/Sm-Ce (0.6) > Ni/Pr-Ce (0.3) > Ni/Ce (0.09). Though, our XPS studies showed that the preference of the dopant elements,  $Pr^{3+}$ ,  $Sm^{3+}$  and  $Mg^{2+}$ , to reside on the surface follows the  $Pr^{3+}$  (3.4 at.%) >  $Sm^{3+}$  (2.6 at.%) >  $Mg^{2+}$  (2.5at. %) order. This allows us to propose that in the case of Ni/Pr-Ce catalyst more surface oxygen vacancies can be found (e.g.  $Ce^{4+}$ -Ov- $Pr^{3+}$  entities), the latter being accessible sites for the  $CO_2$  activation. Additionally, the not direct correlation of the population of the oxygen vacant sites with the activity has also been reported in oxidation reactions [132].

Moreover, the investigation of acid-basic properties showed that the addition of the promoters ( $Sm^{3+}$ ,  $Pr^{3+}$  and  $Mg^{2+}$ ) not only increased the total population of basic sites of  $CeO_2$ , but it predominantly increased the moderate basic sites. This in turn lead to the improvement of the  $CO_2$  methanation reaction via the increased adsorption of  $CO_2$ , which can be bound forming structures, such as covalent carbonates, hydrogen carbonates and then bidentate carbonates and finally to their hydrogenation to produce methane [122]. Lastly, all catalytic samples showed excellent catalytic stability in terms of  $CO_2$  conversion and  $CH_4$  selectivity during the time on stream experiments. This behavior is related to the stabilization of the active sites, with the addition of rare ( $Sm^{3+}$  and  $Pr^{3+}$ ) or alkaline  $Mg^{2+}$  metal cations, which decreased the impact of sintering.

#### 4. Conclusions

In this work, the catalytic performance, in terms of activity and stability, of Ni catalysts based on Sm-Ce, Pr-Ce and Mg-Ce was compared with a Ni/Ce catalyst for the  $CO_2$  methanation reaction. The supporting materials were synthesized using the microwave assisted sol-gel method. To the best of our knowledge, this is the first time that ceria promoted with  $Sm^{3+}$ ,  $Pr^{3+}$  or MgO have been used as supporting material for Ni based catalysts in the  $CO_2$  methanation reaction. Moreover, this is also the first time that this particular support preparation method has been used for the reaction at hand. From the results presented herein, it was shown that the addition of  $Sm^{3+}$  or  $Pr^{3+}$ , incorporated into the lattice of  $CeO_2$ , generated oxygen vacancies, but the Ni/Pr-Ce catalyst was found to possess more surface oxygen vacancies, e.g.,  $Ce^{4+}$ -Ov- $Pr^{3+}$  entities). Moreover, modification of  $CeO_2$  using  $Sm^{3+}$  or  $Pr^{3+}$  restricted the agglomeration of nickel active sites and led to the genesis of Lewis basic positions. These characteristics improved the hydrogenation reaction at lower temperature (10–40% increase of the conversion). On the other hand, the addition of  $Mg^{2+}$  resulted at strong metal support interactions reinforcing the resistance of the Ni/Mg-Ce catalyst against sintering. Moreover, the addition of  $Sm^{3+}$ ,  $Pr^{3+}$  and  $Mg^{2+}$  increased the overall basicity and the moderate adsorption sites and led to the formation of smaller Ni nano particles; these physico-chemical properties enhanced  $CO_2$  methanation reaction. Finally, the activity experiments showed that at low reaction temperature (350 °C) and at WHSV = 25,000 mL  $g^{-1} h^{-1}$ ,  $H_2/CO_2 = 4:1$  the Ni/Pr-Ce showed the highest catalytic performance in terms of  $CO_2$  conversion (54.4%) and  $CH_4$  yield (54.4%) and selectivity (100%). The TOF values were found to follow the order Ni/Pr-Ce > Ni/Mg-Ce > Ni/Sm-Ce > Ni/Ce.

#### CRedit authorship contribution statement

**G.I. Siakavelas:** Conceptualization, Methodology, Validation, Investigation, Writing - original draft, Funding acquisition. **N.D. Charisiou:** Investigation, Writing - original draft, Writing - review & editing, Supervision, Project administration. **S. Alkhoori:** Investigation. **A.A. Alkhoori:** Investigation. **V. Sebastian:** Investigation. **S.J. Hinder:** Investigation. **M.A. Baker:** Investigation, Writing - review & editing. **I.V. Yentekakis:** Writing - review & editing, Funding acquisition. **K. Polychronopoulou:** Investigation, Writing - review & editing, Funding acquisition. **M.A. Goula:** Writing - review & editing, Supervision, Project administration, Funding acquisition.

#### Declaration of Competing Interest

None.

#### Acknowledgments

GIS is grateful for financial support by Greece and ESF through the Operational Programme «Human Resources Development, Education and Lifelong Learning» in the context of the project “Strengthening Human Resources Research Potential via Doctorate Research” (MIS-5000432), implemented by the State Scholarships Foundation (IKY). NDC is grateful to the Research Committee of UOWM for financial support through grant no. 80304. IVY and MAG are grateful for financial support from the European Union and Greek national funds through the operational program Competitiveness, Entrepreneurship and Innovation, under the call Research-Create-Innovate (Project code: T1EDK-00782). SAK, AAK and KP acknowledge the financial support from the Abu Dhabi Department of Education and Knowledge (ADEK) under the AARE 2019-233 grant and support by the Khalifa University of Science and Technology under Award No. RC2-2018-024.

#### Appendix A. Supplementary data

Supplementary material related to this article can be found, in the online version, at doi:<https://doi.org/10.1016/j.apcatb.2020.119562>.

#### References

- X. Wang, H. Shi, J.H. Kwak, J. Szanyi, Mechanism of  $CO_2$  hydrogenation on Pd/ $Al_2O_3$  catalysts: kinetics and transient DRIFTS-MS studies, *ACS Catal.* 5 (2015) 6337–6349, <https://doi.org/10.1021/acscatal.5b01464>.
- S. Akamaru, T. Shimazaki, M. Kubo, T. Abe, Density functional theory analysis of methanation reaction of  $CO_2$  on Ru nanoparticle supported on  $TiO_2$  (101), *Appl. Catal. A* 470 (2014) 405–411, <https://doi.org/10.1016/j.apcata.2013.11.016>.
- A. Westermann, B. Azambre, M.C. Bacariza, I. Graça, M.F. Ribeiro, J.M. Lopes, C. Henriques, Insight into  $CO_2$  methanation mechanism over NiUSY zeolites: an operand IR study, *Appl. Catal. B* 174–175 (2015) 120–125, <https://doi.org/10.1016/j.apcatb.2015.02.026>.
- S.N. Bukhari, C.C. Chong, L.P. The, D.V.N. Vo, N. Ainirazali, S. Triwahyono, A.A. Jalil, H.D. Setiabud, Promising hydrothermal technique for efficient  $CO_2$  methanation over Ni/SBA-15, *Int. J. Hydrog. Energ.* 44 (2019) 20792–20804, <https://doi.org/10.1016/j.ijhydene.2018.07.018>.
- G. Du, S. Lim, Y. Yang, C. Wang, L. Pfefferle, G.L. Haller, Methanation of carbon dioxide on Ni-incorporated MCM-41 catalysts: the influence of catalyst pretreatment and study of steady-state reaction, *J. Catal.* 249 (2007) 370–379, <https://doi.org/10.1016/j.jcat.2007.03.029>.
- B. Miao, S.S.K. Ma, X. Wang, H. Su, S.H. Chan, Catalysis mechanisms of  $CO_2$  and CO methanation, *Catal. Sci. Technol.* 6 (2016) 4048–4058, <https://doi.org/10.1039/C6CY00478D>.
- P. Panagiotopoulou, Hydrogenation of  $CO_2$  over supported noble metal catalysts, *Appl. Catal. A* 542 (2017) 63–70, <https://doi.org/10.1016/j.apcata.2017.05.026>.
- S. Toemen, W.W.A. Bakar, R. Ali, Effect of ceria and strontia over Ru/Mn/ $Al_2O_3$  catalyst: catalytic methanation, physicochemical and mechanistic studies, *J. CO<sub>2</sub> Util.* 13 (2016) 38–49, <https://doi.org/10.1016/j.jcou.2015.11.005>.
- D. Thelert, S. Souentie, A. Siokou, A. Katsaounis, C.G. Vayenas, Hydrogenation of  $CO_2$  over Ru/YSZ electropromoted catalysts, *ACS Catal.* 2 (2012) 770–780, <https://doi.org/10.1021/cs300072a>.
- J.H. Kwak, L. Kovarik, J. Szanyi,  $CO_2$  reduction on supported Ru/ $Al_2O_3$  catalysts: cluster size dependence of product selectivity, *ACS Catal.* 3 (2013) 2449–2455, <https://doi.org/10.1021/cs400381f>.
- A. Karelavic, P. Ruiz,  $CO_2$  hydrogenation at low temperature over Rh/ $\gamma$ - $Al_2O_3$  catalysts: effect of the metal particle size on catalytic performances and reaction mechanism, *Appl. Catal. B* 113–114 (2012) 237–249, <https://doi.org/10.1016/j.apcatb.2011.11.043>.
- J.N. Park, E.W. McFarland, A highly dispersed Pd-Mg/ $SiO_2$  catalyst active for methanation of  $CO_2$ , *J. Catal.* 266 (2009) 92–97, <https://doi.org/10.1016/j.jcat.2009.05.018>.
- J.H. Kwak, L. Kovarik, J. Szanyi, Heterogeneous catalysis on atomically dispersed supported metals:  $CO_2$  reduction on multifunctional Pd catalysts, *ACS Catal.* 3 (2013) 2094–2100, <https://doi.org/10.1021/cs400139z>.
- F. Solymsi, A. Erdöhelyi, Hydrogenation of  $CO_2$  to  $CH_4$  over alumina-supported noble metals, *J. Mol. Catal.* 8 (1980) 471–474, [https://doi.org/10.1016/0304-5102\(80\)80086-1](https://doi.org/10.1016/0304-5102(80)80086-1).
- X. Jia, X. Zhang, N. Rui, X. Hu, C.J. Liu, Structural effect of Ni/ $ZrO_2$  catalyst on  $CO_2$  methanation with enhanced activity, *Appl. Catal. B* 244 (2019) 159–169, <https://doi.org/10.1016/j.apcatb.2018.11.024>.
- X. Wang, L. Zhu, Y. Liu, S. Wang,  $CO_2$  methanation on the catalyst of Ni/MCM-41

- promoted with CeO<sub>2</sub>, *Sci. Total Environ.* 625 (2018) 686–695, <https://doi.org/10.1016/j.scitotenv.2017.12.308>.
- [17] T.A. Le, M.S. Kim, S.H. Lee, T.W. Kim, E.D. Park, CO and CO<sub>2</sub> methanation over supported Ni catalysts, *Catal. Today* 293–294 (2017) 89–96, <https://doi.org/10.1016/j.cattod.2016.12.036>.
- [18] S. Ewald, M. Kolbeck, T. Kratky, M. Wolf, O. Hinrichsen, On the deactivation of Ni-Al catalysts in CO<sub>2</sub> methanation, *Appl. Catal. A* 570 (2019) 376–386, <https://doi.org/10.1016/j.apcata.2018.10.033>.
- [19] C. Mebrahtu, S. Abate, S. Perathoner, S. Chen, G. Centi, CO<sub>2</sub> methanation over Ni catalysts based on ternary and quaternary mixed oxide: a comparison and analysis of the structure-activity relationships, *Catal. Today* 304 (2018) 181–189, <https://doi.org/10.1016/j.cattod.2017.08.060>.
- [20] K. Stangeland, D. Kalai, H. Li, Z. Yu, CO<sub>2</sub> Methanation: the effect of catalysts and reaction conditions, *Energ. Proc.* 105 (2017) 2022–2027, <https://doi.org/10.1016/j.egypro.2017.03.577>.
- [21] M.C. Bacariza, I. Graça, S.S. Bebbiano, J.M. Lopes, C. Henriques, Micro-and mesoporous supports for CO<sub>2</sub> methanation catalysts: a comparison between SBA-15, MCM-41 and USY zeolite, *Chem. Eng. Sci.* 175 (2018) 72–83, <https://doi.org/10.1016/j.ces.2017.09.027>.
- [22] Kim M.S. Le T.A, S.H. Lee, E.D. Park, CO and CO<sub>2</sub> methanation over supported cobalt catalysts, *Top. Catal.* 60 (2017) 714–720, <https://doi.org/10.1007/s11244-017-0788-y>.
- [23] A.C. Ferreira, J.B. Branco, Methanation of CO<sub>2</sub> over nanostructured nickel-4f block element bimetallic oxides, *Int. J. Hydrog. Energy* 44 (2019) 6505–6513, <https://doi.org/10.1016/j.ijhydene.2019.01.160>.
- [24] S. Hwang, J. Lee, U.G. Hong, J.G. Seo, J.C. Jung, D.J. Koh, H. Lim, C. Byun, I.K. Song, Methane production from carbon monoxide and hydrogen over nickel-alumina xerogel catalyst: effect of nickel content, *J. Ind. Eng. Chem.* 17 (2011) 154–157, <https://doi.org/10.1016/j.jiec.2010.12.015>.
- [25] M. Yamasaki, M. Komori, E. Akiyama, H. Habazaki, A. Kawashima, K. Asami, K. Hashimoto, CO<sub>2</sub> methanation catalysts prepared from amorphous Ni-Zr-Sm and Ni-Zr-misch metal alloy precursors, *Mater. Sci. Eng. A* 267 (1999) 220–226, [https://doi.org/10.1016/S0921-5093\(99\)00095-00097](https://doi.org/10.1016/S0921-5093(99)00095-00097).
- [26] N.D. Charisiou, K.N. Papageridis, L. Tzounis, V. Sebastian, M.A. Baker, S.J. Hinder, M. AlKetbi, K. Polychronopoulou, M.A. Goula, Ni supported on CaO-MgO-Al<sub>2</sub>O<sub>3</sub> as a highly selective and stable catalyst for H<sub>2</sub> production via the glycerol steam reforming reaction, *Int. J. Hydrog. Energy* 44 (2019) 256–273, <https://doi.org/10.1016/j.ijhydene.2018.02.165>.
- [27] A.Z. Senseni, F. Meshkani, M. Rezaei, Steam reforming of glycerol on mesoporous nanocrystalline Ni/Al<sub>2</sub>O<sub>3</sub> catalysts for H<sub>2</sub> production, *Int. J. Hydrog. Energy* 41 (2016) 20137–20146, <https://doi.org/10.1016/j.ijhydene.2016.08.046>.
- [28] S. Aghamohammadi, M. Haghghi, M. Maleki, N. Rahemi, Sequential impregnation vs. Sol-gel synthesized Ni/Al<sub>2</sub>O<sub>3</sub>-CeO<sub>2</sub> nanocatalyst for dry reforming of methane: effect of synthesis method and support promotion, *Mol. Catal.* 431 (2017) 39–48, <https://doi.org/10.1016/j.mcat.2017.01.012>.
- [29] M. Li, A.C. van Veen, Tuning the catalytic performance of Ni-catalysed dry reforming of methane and carbon deposition via Ni-CeO<sub>2-x</sub> interaction, *Appl. Catal. B* 237 (2018) 641–648, <https://doi.org/10.1016/j.apcatb.2018.06.032>.
- [30] B. Li, B. Zhang, Q. Guan, S. Chen, P. Ning, Activity of Ni/CeO<sub>2</sub> catalyst for gasification of phenol in supercritical water, *Int. J. Hydrog. Energy* 43 (2018) 19010–19018, <https://doi.org/10.1016/j.ijhydene.2018.08.105>.
- [31] I.V. Yentekakis, G. Goula, M. Hatzisymeon, I. Betsi-Argyropoulou, G. Botzolaki, K. Kousi, D.I. Kondarides, M.J. Taylor, C.M.A. Parlett, A. Osatiastiani, G. Kyriakou, J.P. Holgado, R.M. Lambert, Effect of support oxygen storage capacity on the catalytic performance of Rh nanoparticles for CO<sub>2</sub> reforming of methane, *Appl. Catal. B* 243 (2019) 490–501, <https://doi.org/10.1016/j.apcatb.2018.10.048>.
- [32] G. Goula, G. Botzolaki, A. Osatiastiani, C.M.A. Parlett, G. Kyriakou, R.M. Lambert, I.V. Yentekakis, Oxidative thermal sintering and redispersion of Rh nanoparticles on supports with high oxygen ion lability, *Catalysts* 9 (2019) 541, <https://doi.org/10.3390/catal9060541>.
- [33] K. Polychronopoulou, A.F. Zedan, M.S. Katsiotis, M.A. Baker, A.A. Alkhoori, Y. Sijam, S.J. Qaradawi Al Hinder, J. AlHassan Saeed, Rapid microwave assisted sol-gel synthesis of CeO<sub>2</sub> and Ce<sub>0.8</sub>Sm<sub>0.2</sub>O<sub>2</sub> nanoparticle catalysts for CO oxidation, *Mol. Catal. A* 428 (2017) 41–55, <https://doi.org/10.1016/j.molcata.2016.11.039>.
- [34] D. Gamarra, A.L. Camara, M. Monte, S.B. Rasmussen, L.E. Chinchilla, A.B. Hungria, G. Munuera, N. Gyorffy, Z. Schay, V.C. Corberán, J.C. Conesa, A. Martínez-Arias, Preferential oxidation of CO in excess H<sub>2</sub> over CuO/CeO<sub>2</sub> catalysts: characterization and performance as a function of the exposed face present in the CeO<sub>2</sub> support, *Appl. Catal. B* 130–131 (2013) 224–238, <https://doi.org/10.1016/j.apcatb.2012.11.008>.
- [35] M. AlKetbi, K. Polychronopoulou, A.F. Zedan, V. Sebastiani, M.A. Baker, A. Alkhoori, M.A. Jaoude, O. Alnuaimi, S.S. Hinder, A. Tharalekshmy, A.S. AlJaber, Tuning the activity of Cu-containing rare earth oxide catalysts for CO oxidation reaction: cooling while heating paradigm in microwave-assisted synthesis, *Mater. Res. Bull.* 108 (2018) 142–150, <https://doi.org/10.1016/j.materresbull.2018.08.045>.
- [36] I.V. Yentekakis, G. Goula, P. Panagiotopoulou, S. Kampouri, M.J. Taylor, G. Kyriakou, R.M. Lambert, Stabilization of catalyst particles against sintering on oxide supports with high oxygen ion lability exemplified by Ir-catalyzed decomposition of N<sub>2</sub>O, *Appl. Catal. B* 192 (2016) 357–364, <https://doi.org/10.1016/j.apcatb.2016.04.011>.
- [37] M.F. Luo, Z.L. Yan, L.Y. Jin, Structure and redox properties of Ce<sub>x</sub>Pr<sub>1-x</sub>O<sub>2-δ</sub> mixed oxides and their catalytic activities for CO, CH<sub>3</sub>OH and CH<sub>4</sub> combustion, *J. Mol. Catal. A* 260 (2006) 157–162, <https://doi.org/10.1016/j.molcata.2006.07.012>.
- [38] I. Luisetto, S. Tuti, C. Romano, M. Boaro, E. Di Bartolomeo, J.K. Kesavan, S.M.S. Kumar, K. Selvakumar, Dry reforming of methane over Ni supported on doped CeO<sub>2</sub>: new insight on the role of dopants for CO<sub>2</sub> activation, *J. CO<sub>2</sub> Util.* 30 (2019) 63–78, <https://doi.org/10.1016/j.jcou.2019.01.006>.
- [39] L.M. Gomez-Sainero, R.T. Baker, A.J. Vizcaíno, S.M. Francis, J.A. Calles, L.S. Metcalfe, J.J. Rodriguez, Steam reforming of methanol with Sm<sub>2</sub>O<sub>3</sub>-CeO<sub>2</sub>-supported palladium catalysts: influence of the thermal treatments of catalyst and support, *Ind. Eng. Chem. Res.* 48 (2009) 8364–8372, <https://doi.org/10.1021/ie900630z>.
- [40] M. AlKetbi, K. Polychronopoulou, M.A. Jaoude, M.A. Vasiliades, V. Sebastian, S.J. Hinder, M.A. Baker, A.F. Zedan, A.M. Efstathiou, Cu-Ce-La-Ox as efficient CO oxidation catalysts: effect of Cu content, *Appl. Surf. Sci.* 505 (2020) 144474, <https://doi.org/10.1016/j.apsusc.2019.144474>.
- [41] K. Polychronopoulou, N.D. Charisiou, G.I. Siakavelas, A.A. Alkhoori, V. Sebastian, S.J. Hinder, M.A. Baker, M.A. Goula, Ce-Sm-xCu cost-efficient catalysts for H<sub>2</sub> production through the glycerol steam reforming reaction, *Sustain. Energ. Fuels* 3 (2019) 673–691, <https://doi.org/10.1039/C8SE00388B>.
- [42] M. Khajenoori, M. Rezaei, F. Meshkani, Dry reforming over CeO<sub>2</sub>-promoted Ni/MgO nano-catalyst: Effect of Ni loading and CH<sub>4</sub>/CO<sub>2</sub> molar ratio, *J. Ind. Eng. Chem.* 21 (2015) 717–722, <https://doi.org/10.1016/j.jiec.2014.03.043>.
- [43] M. Saito, M. Itoh, J. Iwamoto, C.Y. Li, K. Machida, Synergistic effect of MgO and CeO<sub>2</sub> as a support for ruthenium catalysts in Ammonia synthesis, *Catal. Lett.* 106 (2006) 107–110, <https://doi.org/10.1007/s10562-005-9615-3>.
- [44] S. Shi, J.-Y. Hwang, Microwave-assisted wet chemical synthesis: advantages, significance, and steps to industrialization, *J. Miner. Mater. Char. Eng.* 2 (2003) 101–110, <https://doi.org/10.4236/jmmce.2003.22009>.
- [45] S. Komarneni, Nanophase materials by hydrothermal, microwave-hydrothermal and microwave-solvothermal methods, *Curr. Sci.* 85 (2003) 1730–1734.
- [46] S. Komarneni, H. Katsuki, Nanophase materials by a novel microwave-hydrothermal process, *Pure Appl. Chem.* 74 (9) (2002) 1537–1543, <https://doi.org/10.1351/pac200274091537>.
- [47] K. Polychronopoulou, A.F. Zedan, M. AlKetbi, S. Stephen, M. Ather, M.S. Katsiotis, J. Arvanitidis, D. Christofilos, A.F. Isakov, S. AlHassan, Tailoring the efficiency of an active catalyst for CO abatement through oxidation reaction: the case study of samarium-doped ceria, *J. Environ. Chem. Eng.* 1 (2018) 266–280, <https://doi.org/10.1016/j.jecec.2017.12.001>.
- [48] K.N. Papageridis, N.D. Charisiou, S.L. Douvartzides, V. Sebastian, S.J. Hinder, M.A. Baker, S. Alkhoori, K. Polychronopoulou, M.A. Goula, Effect of operating parameters on the selective catalytic deoxygenation of palm oil to produce renewable diesel over Ni supported on Al<sub>2</sub>O<sub>3</sub>, ZrO<sub>2</sub> and SiO<sub>2</sub> catalysts, *Fuel Process. Technol.* 209 (2020) 106547, <https://doi.org/10.1016/j.fuproc.2020.106547>.
- [49] B. Zhang, D. Li, X. Wang, Catalytic performance of La-Ce-O mixed oxide for combustion of methane, *Catal. Today* 158 (3–4) (2010) 348–353, <https://doi.org/10.1016/j.cattod.2010.04.019>.
- [50] A. Gurbani, J.L. Ayastuy, M.P. Gonzalez-Marcos, M.A. Gutierrez-Ortiz, CuO-CeO<sub>2</sub> catalysts synthesized by various methods: comparative study of redox properties, *Int. J. Hydrog. Energy* 35 (20) (2010) 11582–11590, <https://doi.org/10.1016/j.ijhydene.2010.04.045>.
- [51] C. Liang, X. Hu, T. Wei, P. Jia, Z. Zhang, D. Dong, S. Zhang, Q. Liu, G. Hu, Methanation of CO<sub>2</sub> over Ni/Al<sub>2</sub>O<sub>3</sub> modified with alkaline earth metals: impacts of oxygen vacancies on catalytic activity, *Int. J. Hydrog. Energy* 44 (2019) 8197–8213, <https://doi.org/10.1016/j.ijhydene.2019.02.014>.
- [52] F. Wang, S. He, H. Chen, B. Wang, L. Zheng, M. Wei, D.G. Evans, X. Duan, Active site dependent reaction mechanism over Ru/CeO<sub>2</sub> catalyst toward CO<sub>2</sub> methanation, *JACS* 138 (2016) 6298–6305, <https://doi.org/10.1021/jacs.6b02762>.
- [53] K. Xavier, R. Sreekala, K. Rashid, K. Yusuff, B. Sen, Doping effects of cerium oxide on Ni/Al<sub>2</sub>O<sub>3</sub> catalysts for methanation, *Catal. Today* 49 (1999) 17–21, [https://doi.org/10.1016/S0920-5861\(98\)00403-00409](https://doi.org/10.1016/S0920-5861(98)00403-00409).
- [54] W.D. Callister, D.G. Rethwisch, *Materials Science and Engineering Textbook*, John Wiley & Sons Inc, NY, USA, 2014.
- [55] H. Nitani, T. Nakagawa, M. Yamanouchi, T. Osuki, M. Yuya, T.A. Yamamoto, XAFS and XRD study of ceria doped with Pr, Nd or Sm, *Matter. Lett.* 58 (2004) 2076–2081, <https://doi.org/10.1016/j.matlet.2004.01.005>.
- [56] T. Taniguchi, T. Watanabe, N. Sugiyama, A.K. Subramani, H. Wagata, N. Matsushita, M. Yoshimura, Identifying defects in ceria-based nanocrystals by UV resonance Raman spectroscopy, *J. Phys. Chem. C* 113 (2009) 19789–19793, <https://doi.org/10.1021/jp9049457>.
- [57] A. Nakajima, A. Yoshihara, M. Ishigame, Defect-Induced Raman Spectra in Doped CeO<sub>2</sub>, *Phys. Rev. B* 50 (1994) 13297–13307, <https://doi.org/10.1103/PhysRevB.50.13297>.
- [58] D. Stoian, F. Medina, A. Urakawa, Improving the stability of CeO<sub>2</sub> catalyst by rare earth metal promotion and molecular insights in the dimethyl carbonate synthesis from CO<sub>2</sub> and methanol with 2-Cyanopyridine, *ACS Catal.* 8 (2018) 3181–3193, <https://doi.org/10.1021/acscatal.7b04198>.
- [59] N.D. Charisiou, G. Siakavelas, K.N. Papageridis, A. Baklavariadis, L. Tzounis, K. Polychronopoulou, M.A. Goula, Hydrogen production via the glycerol steam reforming reaction over nickel supported on alumina and lanthana-alumina catalysts, *Int. J. Hydrog. Energy* 42 (2017) 13039–13060, <https://doi.org/10.1016/j.ijhydene.2017.04.048>.
- [60] K. Zhang, G. Zhou, J. Li, T. Cheng, The electronic effects of Pr on La<sub>1-x</sub>Pr<sub>x</sub>NiAl<sub>11</sub>O<sub>19</sub> for CO<sub>2</sub> reforming of methane, *Catal. Commun.* 10 (2009) 1816–1820, <https://doi.org/10.1016/j.catcom.2009.06.007>.
- [61] M.A. Goula, N.D. Charisiou, K.N. Papageridis, A. Delimitis, E. Pachatouridou, E.F. Iliopoulou, Nickel on alumina catalysts for the production of hydrogen rich mixtures via the biogas dry reforming reaction: influence of the synthesis method, *Int. J. Hydrog. Energy* 40 (2015) 9183–9200, <https://doi.org/10.1016/j.ijhydene.2015.05.129>.

- [62] J. Rouquerol, F. Rouquerol, P. Llewellyn, G. Maurin, K.S. Sing, *Adsorption by Powders and Porous Solids: Principles, Methodology and Applications*, Academic Press, Cambridge, MA, USA, 1999.
- [63] K.S.W. Sing, D.H. Everett, R.A.W. Hall, L. Moscou, R.A. Pierotti, J. Rouquerol, T. Siemieniowska, Reporting physisorption data for gas/solid systems with special reference to the determination of surface area and porosity, *IUPAC 57* (1985) 603–619.
- [64] N.D. Charisiou, G. Siakavelas, B. Dou, V. Sebastian, S.J. Hinder, M.A. Baker, K. Polychronopoulou, M.A. Goula, Nickel supported on AlCeO<sub>3</sub> as a highly selective and stable catalyst for hydrogen production via the glycerol steam reforming reaction, *Catalysts* 9 (2019) 411, <https://doi.org/10.3390/catal9050411>.
- [65] A. Westermann, B. Azambre, M.C. Bacariza, I. Graca, M.F. Ribeiro, J.M. Lopes, C. Henriques, The promoting effect of Ce in the CO<sub>2</sub> methanation performances on NiUSY zeolite: a FTIR in Situ/Operando study, *Catal. Today* 283 (2017) 74–81, <https://doi.org/10.1016/j.cattod.2016.02.031>.
- [66] P. Kumar, V.C. Srivastava, I.M. Mishra, Synthesis and characterization of Ce-La oxides for the formation of dimethyl carbonate by transesterification of propylene carbonate, *Catal. Commun.* 60 (2015) 27–31, <https://doi.org/10.1016/j.catcom.2014.11.006>.
- [67] K. Zhao, W. Wang, Z. Li, Highly efficient Ni/ZrO<sub>2</sub> catalysts prepared via combustion method for CO<sub>2</sub> methanation, *J. CO<sub>2</sub> Util.* 16 (2016) 236–244, <https://doi.org/10.1016/j.jcou.2016.07.010>.
- [68] S. Li, G. Liu, S. Zhang, K. An, Z. Ma, L. Wang, Y. Liu, Cerium-modified Ni-La<sub>2</sub>O<sub>3</sub>/ZrO<sub>2</sub> for CO<sub>2</sub> methanation, *J. Energy Chem.* 43 (2020) 155–164, <https://doi.org/10.1016/j.jechem.2019.08.024>.
- [69] T. Staudt, Y. Lykhach, N. Tsud, T. Skala, K.C. Prince, V. Matolin, J. Libuda, Ceria reoxidation by CO<sub>2</sub>: a model study, *J. Catal.* 275 (2010) 181–185, <https://doi.org/10.1016/j.jcat.2010.07.032>.
- [70] Z. Cheng, B.J. Sherman, C.S. Lo, Carbon dioxide activation and dissociation on ceria (110): a density functional theory study, *J. Chem. Phys.* 138 (2013) 014702, <https://doi.org/10.1063/1.4773248>.
- [71] Q. Fu, A. Weber, M. Flytzani-Stephanopoulos, Nanostructured Au-CeO<sub>2</sub> catalysts for low-temperature water-gas shift, *Catal. Lett.* 77 (2001) 87–95, <https://doi.org/10.1023/A:1012666128812>.
- [72] C. Italiano, J. Llorca, L. Pino, M. Ferraro, V. Antonucci, A. Vita, CO and CO<sub>2</sub> methanation over Ni catalysts supported on CeO<sub>2</sub>, Al<sub>2</sub>O<sub>3</sub> and Y<sub>2</sub>O<sub>3</sub> oxides, *Appl. Catal. B* 264 (2020) 118494, <https://doi.org/10.1016/j.apcatb.2019.118494>.
- [73] L. Xu, H. Song, L. Chou, Mesoporous nanocrystalline ceria-zirconia solid solutions supported nickel based catalysts for CO<sub>2</sub> reforming of CH<sub>4</sub>, *Int. J. Hydrog. Energy* 37 (2012) 18001–18020, <https://doi.org/10.1016/j.ijhydene.2012.09.128>.
- [74] W. Liu, W. Wang, K. Tang, J. Guo, Y. Ren, Y. Wang, S. Wang, L. Feng, Y. Yang, The promoting influence of nickel species in the controllable synthesis and catalytic properties of nickel-ceria catalysts, *Catal. Sci. Technol.* 6 (2016) 2427–2434, <https://doi.org/10.1039/C5CY01241D>.
- [75] M.C. Le, K.L. Van, T.H. Nguyen, N.H. Nguyen, The impact of Ce-Zr addition on nickel dispersion and catalytic behavior for CO<sub>2</sub> methanation of Ni/AC catalyst at low temperature, *J. Chem.* (2017) 4361056, <https://doi.org/10.1155/2017/4361056>.
- [76] J.B. Branco, P.E. Brito, A.C. Ferreira, Methanation of CO<sub>2</sub> over nickel-lanthanide bimetallic oxides supported on silica, *Chem. Eng. J.* 380 (2020) 122465, <https://doi.org/10.1016/j.cej.2019.122465>.
- [77] R.K. Singha, A. Shukla, A. Yadav, L.N.S. Konathala, R. Bal, Effect of metal-support interaction on activity and stability of Ni-CeO<sub>2</sub> catalyst for partial oxidation of methane, *Appl. Catal. B* 202 (2017) 473–488, <https://doi.org/10.1016/j.apcatb.2016.09.060>.
- [78] M.A. Goula, N.D. Charisiou, G. Siakavelas, L. Tzounis, I. Tsiaoussis, P. Panagiotopoulou, G. Goula, I.V. Yentekakis, Syngas production via the biogas dry reforming reaction over Ni supported on zirconia modified with CeO<sub>2</sub> or La<sub>2</sub>O<sub>3</sub> catalysts, *Int. J. Hydrog. Energy* 42 (2017) 13724–13740, <https://doi.org/10.1016/j.ijhydene.2016.11.196>.
- [79] Q. Shi, C. Liu, W. Chen, Hydrogen production from steam reforming of ethanol over Ni/MgO-CeO<sub>2</sub> catalyst at low temperature, *J. Rare Earth.* 27 (2009) 948–954, [https://doi.org/10.1016/S1002-0721\(08\)60368-3](https://doi.org/10.1016/S1002-0721(08)60368-3).
- [80] S. Ewald, S. Standl, O. Hinrichsen, Characterization of nickel catalysts with transient methods, *Appl. Catal. A* 549 (2018) 93–101, <https://doi.org/10.1016/j.apcata.2017.09.023>.
- [81] S. Smeds, T. Salmi, L.P. Lindfors, O. Krause, Chemisorption and TPD studies of hydrogen on Ni/Al<sub>2</sub>O<sub>3</sub>, *Appl. Catal. A* 144 (1996) 177–194, [https://doi.org/10.1016/0926-860X\(96\)00103-2](https://doi.org/10.1016/0926-860X(96)00103-2).
- [82] S. Velu, S.K. Gangwal, Synthesis of alumina supported nickel nanoparticle catalysts and evaluation of nickel metal dispersions by temperature programmed desorption, *Solid State Ion.* 177 (2006) 803–811, <https://doi.org/10.1007/s11051-016-3385-2>.
- [83] L. Torrente-Murciano, The importance of particle-support interaction on particle size determination by gas chemisorption, *J. Nanopart. Res.* 18 (2016) 87, <https://doi.org/10.1007/s11051-016-3385-2>.
- [84] Z.Y. Li, N.P. Young, M. Di Vece, S. Palomba, R.E. Palmer, A.L. Bleloch, B.C. Curley, R.L. Johnston, J. Jiang, J. Yuan, Three-dimensional atomic-scale structure of size-selected gold nanoclusters, *Nature* 451 (2018) 46–48, <https://doi.org/10.1038/nature06470>.
- [85] L.M. Molina, S. Lee, K. Sell, G. Barcaro, A. Fortunelli, B. Lee, S. Seifert, R.E. Winans, J.W. Elam, M.F. Pellin, I. Barke, Oeynhausen V. von, Y. Lei, R.J. Meyer, J.A. Alonso, A.F. Rodriguez, A. Kleibert, S. Giorgio, C.R. Henry, K.H. Meiwes-Broer, S. Vajda, Size-dependent selectivity and activity of silver nanoclusters in the partial oxidation of propylene to propylene oxide and acrolein: a joint experimental and theoretical study, *Catal. Today* 160 (2011) 116–130, <https://doi.org/10.1016/j.cattod.2010.08.022>.
- [86] I.V. Yudanov, R. Sahnoun, K.M. Neyman, N. Rosch, J. Hoffmann, S. Schaueremann, V. Johaneck, H. Unterhalt, G. Rupprechter, J. Libuda, H.J. Freund, CO adsorption on Pd nanoparticles: density functional and vibrational spectroscopy studies, *J. Phys. Chem. B* 107 (2003) 255–264, <https://doi.org/10.1021/jp022052b>.
- [87] C. Guzman, G. Del Angel, R. Gomez, F. Galindo, R. Zanella, G. Torres, C. Angeles-Chavez, J.L.G. Fierro, Gold particle size determination on Au/TiO<sub>2</sub>-CeO<sub>2</sub> catalysts by means of carbon monoxide, hydrogen chemisorption and transmission electron microscopy, *J. Nano Res.* 5 (2009) 13–23, <https://doi.org/10.3390/nano9030344>.
- [88] K.N. Papageridis, N.D. Charisiou, S.L. Douvartzides, V. Sebastian, S.J. Hinder, M.A. Baker, K. Polychronopoulou, M.A. Goula, Effect of operating parameters on the selective catalytic deoxygenation of palm oil to produce renewable diesel over Ni supported on Al<sub>2</sub>O<sub>3</sub>, ZrO<sub>2</sub> and SiO<sub>2</sub> catalysts, *Fuel Process. Technol.* 209 (2020) 106547, <https://doi.org/10.1016/j.fuproc.2020.106547>.
- [89] N.D. Charisiou, G. Siakavelas, L. Tzounis, B. Dou, V. Sebastian, S.J. Hinder, M.A. Baker, K. Polychronopoulou, M.A. Goula, Ni/Y<sub>2</sub>O<sub>3</sub>-ZrO<sub>2</sub> catalyst for hydrogen production through the glycerol steam reforming reaction, *Int. J. Hydrog. Energy* 45 (2020) 10442–10460, <https://doi.org/10.1016/j.ijhydene.2019.04.237>.
- [90] M.C. Biesinger, B.P. Payne, L.W. M.Lau, A. Gerson, Smart R.St.C, X-ray photoelectron spectroscopic chemical state quantification of mixed nickel metal, oxide and hydroxide systems, *Surf. Interface Anal.* 41 (2009) 324–332, <https://doi.org/10.1002/sia.3026>.
- [91] P. Burroughs, A. Hamnett, A.F. Orchard, G. Thornton, Satellite structure in the X-ray photoelectron spectra of some binary and mixed oxides of lanthanum and cerium, *J. Chem. Soc. Dalton Trans.* 17 (1976) 1686–1698, <https://doi.org/10.1039/D79760001686>.
- [92] D.R. Mullins, S.H. Overbury, D.R. Huntley, Electron spectroscopy of single crystal and polycrystalline cerium oxide surfaces, *Surf. Sci.* 409 (1998) 307–319, [https://doi.org/10.1016/S0039-6028\(98\)00257-X](https://doi.org/10.1016/S0039-6028(98)00257-X).
- [93] A. Pfau, K.D. Schierbaum, The electronic structure of stoichiometric and reduced CeO<sub>2</sub> surfaces: an XPS, UPS and HREELS study, *Surf. Sci.* 321 (1994) 71–80, [https://doi.org/10.1016/0039-6028\(94\)90027-2](https://doi.org/10.1016/0039-6028(94)90027-2).
- [94] H. Ogasawara, A. Kotani, R. Potze, G.A. Sawatzky, B.T. Thole, Praseodymium 3d- and 4d-core photoemission spectra of Pr<sub>2</sub>O<sub>3</sub>, *Phys. Rev. B* 44 (1991) 5465, <https://doi.org/10.1103/physrevb.44.5465>.
- [95] A. Mekki, Kh.A. Ziq, D. Holland, C.F. McConville, Magnetic properties of praseodymium ions in Na<sub>2</sub>O-Pr<sub>2</sub>O<sub>3</sub>-SiO<sub>2</sub> glasses, *J. Magn. Mater.* 260 (2003) 60–69, [https://doi.org/10.1016/S0304-8853\(02\)00568-1](https://doi.org/10.1016/S0304-8853(02)00568-1).
- [96] D.D. Sarma, C.N. Rao, XPS studies of oxides of second- and third-row transition metals including rare earths, *J. Electron Spectrosc. Relat. Phenomena* 20 (180) (2020) 25–45, [https://doi.org/10.1016/0368-2048\(80\)85003-1](https://doi.org/10.1016/0368-2048(80)85003-1).
- [97] T.W. Elkins, H.E. Hagelin-Weaver, Oxidative coupling of methane over unsupported and alumina-supported samaria catalysts, *Appl. Catal. A* 454 (2013) 100–114, <https://doi.org/10.1016/j.apcata.2013.01.010>.
- [98] C. Suzuki, J. Kawai, M. Takahashi, A.-H. Vlaicu, H. Adachi, T. Mukoyama, The electronic structure of rare-earth oxides in the creation of the core hole, *Chem. Phys.* 253 (2000) 27–40, [https://doi.org/10.1016/S0301-0104\(99\)00380-00388](https://doi.org/10.1016/S0301-0104(99)00380-00388).
- [99] C.D. Wagner, W.M. Riggs, L.E. Davis, J.F. Moulder, G.E. Muilenberg, *Handbook of X-ray Photoelectron Spectroscopy Physical Electronics Division*, Perkin-Elmer Corporation, Eden Prairie, Minnesota, USA, 1979, <https://doi.org/10.1002/sia.740030412>.
- [100] K. Wu, L. Zhou, C.-J. Jia, L.-D. Sun, C.-H. Yan, Pt-embedded-CeO<sub>2</sub> hollow spheres for enhancing CO oxidation performance, *Mater. Chem. Front.* 1 (2017) 1754–1763, <https://doi.org/10.1039/C7QM00244K>.
- [101] S. Song, H. Wang, A. Song, S. Dong, J. Hao, Sponge phase producing porous CeO<sub>2</sub> for catalytic oxidation of CO, *Chem. Eur. J.* 20 (2014) 9063–9072, <https://doi.org/10.1002/chem.201304836>.
- [102] I. Kuznecova, J. Gusca, Property based ranking of CO and CO<sub>2</sub> methanation catalysts, *Energy. Proceed.* 128 (2017) 255–260, <https://doi.org/10.1016/j.egypro.2017.09.068>.
- [103] C. Vogt, M. Monai, E.B. Sterk, J. Palle, A.E.M. Melcherts, B. Zijlstra, E. Groeneveld, P.H. Berben, J.M. Boerboom, E.J.M. Hensen, F. Meirer, I.A.W. Filot, B.M. Weckhuysen, Understanding carbon dioxide activation and carbon-carbon coupling over nickel, *Nat. Commun.* 10 (2019) 5330, <https://doi.org/10.1038/s41467-019-12858-3>.
- [104] C. Liang, X. Hu, T. Wei, P. Jia, Z. Zhang, D. Dong, S. Zhang, Q. Liu, G. Hu, Methanation of CO<sub>2</sub> over Ni/Al<sub>2</sub>O<sub>3</sub> modified with alkaline earth metals: impacts of oxygen vacancies on catalytic activity, *Inter. J. Hydrog. Energy* 44 (2019) 8197–8213, <https://doi.org/10.1016/j.ijhydene.2019.02.014>.
- [105] J.K. Kesavan, I. Luisetto, S. Tuti, C. Meneghini, G. Iucci, C. Battocchio, S. Mobilio, S. Casciardi, R. Sisto, Nickel supported on YSZ: the effect of Ni particle size on the catalytic activity for CO<sub>2</sub> methanation, *J. CO<sub>2</sub> Util.* 23 (2018) 200–211, <https://doi.org/10.1016/j.jcou.2017.11.015>.
- [106] M.A.A. Aziz, A.A. Jalil, S. Triwahyono, R.R. Mukti, Y.H. Taufiq-Yap, M.R. Sazegar, Highly active Ni-promoted mesostructured silica nanoparticles for CO<sub>2</sub> methanation, *Appl. Catal. B* 147 (2014) 359–368, <https://doi.org/10.1016/j.apcatb.2013.09.015>.
- [107] C. Lamonier, A. Ponchel, A. D'Huysser, L. Jalowiecki-Duhamel, Studies of the cerium-metal-oxygen-hydrogen system (metal = Cu, Ni), *Catal. Today* 50 (1999) 247–259, [https://doi.org/10.1016/S0920-5861\(98\)00507-0](https://doi.org/10.1016/S0920-5861(98)00507-0).
- [108] J.B. Branco, A.C. Ferreira, T.A. Gasche, G. Pimenta, J.P. Leal, Low temperature partial oxidation of methane over bimetallic nickel-Fe block element oxide nanocatalysts, *Adv. Synth. Catal.* 356 (2014) 3048–3058, <https://doi.org/10.1002/adsc.201400102>.
- [109] J.B. Branco, C.J. Dias, A.P. Goncalves, Thermal studies on oxidation-reduction of

- LnCu<sub>2</sub> intermetallic compounds and their catalytic behavior for 2-propanol decomposition, *J. Alloys. Compd.* 478 (2009) 687–693, <https://doi.org/10.1016/j.jallcom.2008.11.113>.
- [110] L. Xu, F. Wang, M. Chen, J. Zhang, K. Yuan, L. Wang, K. Wu, G. Xu, W. Chen, CO<sub>2</sub> methanation over a Ni based ordered mesoporous catalyst for the production of synthetic natural gas, *RSC Adv.* 6 (2016) 28489–28499, <https://doi.org/10.1039/C6RA01139J>.
- [111] M. Aziz, A. Jalil, S. Triwahyono, A. Ahmad, CO<sub>2</sub> methanation over heterogeneous catalysts: recent progress and future prospects, *Green Chem.* 17 (2015) 2647–2663, <https://doi.org/10.1039/C5GC00119F>.
- [112] G. Garbarino, P. Riani, L. Magistri, G. Busca, A study of the methanation of carbon dioxide on Ni/Al<sub>2</sub>O<sub>3</sub> catalysts at atmospheric pressure, *Int. J. Hydrog. Energy* 39 (2014) 11557–11565, <https://doi.org/10.1016/j.ijhydene.2014.05.111>.
- [113] S.Y. Foo, C.K. Cheng, T.-H. Nguyen, E.M. Kennedy, B.Z. Dlugogorski, A.A. Adesina, Carbon deposition and gasification kinetics of used lanthanide-promoted Co-Ni/Al<sub>2</sub>O<sub>3</sub> catalysts from CH<sub>4</sub> dry reforming, *Catal. Commun.* 26 (2012) 183–188, <https://doi.org/10.1016/j.catcom.2012.06.003>.
- [114] P.A. Ussa Aldana, F. Ocampo, K. Kobl, B. Louis, F. Thibault Starzyk, M. Daturi, P. Bazin, S. Thomas, A.C. Roger, Catalytic CO<sub>2</sub> valorization into CH<sub>4</sub> on Ni-based ceria-zirconia. Reaction mechanism by operando IR spectroscopy, *Catal. Today* 215 (2013) 201–207, <https://doi.org/10.1016/j.cattod.2013.02.019>.
- [115] Q.S. Pan, J.X. Peng, T.J. Sun, S. Wang, S.D. Wang, Insight into the reaction route of CO<sub>2</sub> methanation: promotion effect of medium basic sites, *Catal. Commun.* 45 (2014) 74–78, <https://doi.org/10.1016/j.catcom.2013.10.034>.
- [116] T.A. Le, T.W. Kim, S.H. Lee, E.D. Park, Effects of Na content in Na/Ni/SiO<sub>2</sub> and Na/Ni/CeO<sub>2</sub> catalysts for CO and CO<sub>2</sub> methanation, *Catal. Today* 303 (2018) 159–167, <https://doi.org/10.1016/j.cattod.2017.09.031>.
- [117] M.L. Ang, U. Oemar, E.T. Saw, L. Mo, Y. Kathiraser, B.H. Chia, S. Kawi, Highly active Ni/xNa/CeO<sub>2</sub> catalyst for the water - gas shift reaction: effect of sodium on methane suppression, *ACS Catal.* 4 (2014) 3237–3248, <https://doi.org/10.1021/cs500915p>.
- [118] D. Wierzbicki, R. Baran, R. Debek, M. Motak, T. Grzybek, M.E. Galvez, T. Grzybek, M.E. Gálvez, P. Da Costa, The influence of nickel content on the performance of hydrotalcite-derived catalysts in CO<sub>2</sub> methanation reaction, *Int. J. Hydrog. Energy* 42 (2017) 23548–23555, <https://doi.org/10.1016/j.ijhydene.2017.02.148>.
- [119] C. Sun, K. Swirk, D. Wierzbicki, M. Motak, T. Grzybek, P.D. Costa, On the Effect of Yttrium Promotion on Ni-layered Double Hydroxides-derived Catalysts for Hydrogenation of CO<sub>2</sub> to Methane, *In Press* (2020), <https://doi.org/10.1016/j.ijhydene.2020.03.202>.
- [120] W. Yang, Y. Feng, W. Chu, Promotion effect of CaO modification on mesoporous Al<sub>2</sub>O<sub>3</sub>-Supported Ni catalysts for CO<sub>2</sub> methanation, *Int. J. Chem. Eng.* 2016 (2016), <https://doi.org/10.1155/2016/2041821> Article ID 2041821.
- [121] M. Guo, G. Lu, The difference of roles of alkaline-earth metal oxides on silica-supported nickel catalysts for CO<sub>2</sub> methanation, *RSC Adv.* 4 (2014) 58171–58177, <https://doi.org/10.1039/C4RA06202G>.
- [122] N. Perkas, G. Amirian, Z. Zhong, J. Teo, Y. Gofer, A. Gedanken, Methanation of carbon dioxide on Ni catalysts on mesoporous ZrO<sub>2</sub> doped with rare earth oxides, *Catal. Lett.* 130 (2009) 455–462, <https://doi.org/10.1007/s10562-009-9952-9958>.
- [123] G. Zhi, X. Guo, Y. Wang, G. Jin, X. Guo, Effect of La<sub>2</sub>O<sub>3</sub> modification on the catalytic performance of Ni/SiC for methanation of carbon dioxide, *Catal. Commun.* 16 (2011) 56–59, <https://doi.org/10.1016/j.catcom.2011.08.037>.
- [124] G. Garbarino, C. Wang, T. Cavattoni, E. Finocchio, P. Riani, M. Flytzani-Stephanopoulos, G. Busca, A study of Ni/La-Al<sub>2</sub>O<sub>3</sub> catalysts: a competitive system for CO<sub>2</sub> methanation, *Appl. Catal. B* 248 (2019) 286–297, <https://doi.org/10.1016/j.apcatb.2018.12.063>.
- [125] W. Ahmad, M.N. Younis, R. Shawabkeh, S. Ahmed, Synthesis of lanthanide series (La, Ce, Pr, Eu & Gd) promoted Ni/ $\gamma$ -Al<sub>2</sub>O<sub>3</sub> catalysts for methanation of CO<sub>2</sub> at low temperature under atmospheric pressure, *Catal. Commun.* 100 (2017) 121–126, <https://doi.org/10.1016/j.catcom.2017.06.044>.
- [126] L. Bian, L. Zhang, R. Xia, Z. Li, Enhanced low-temperature CO<sub>2</sub> methanation activity on plasma-prepared Ni-based catalyst, *J. Nat. Gas Sci. Eng.* 27 (2015) 1189–1194, <https://doi.org/10.1016/j.jngse.2015.09.066>.
- [127] H. Takano, Y. Kirihata, K. Izumiya, N. Kumagai, H. Habazaki, K. Hashimoto, Highly active Ni/Y-doped ZrO<sub>2</sub> catalysts for CO<sub>2</sub> methanation, *Appl. Surf. Sci.* 388 (2016) 653–663, <https://doi.org/10.1016/j.apsusc.2015.11.187>.
- [128] M.Y.S. Hamid, M.L. Firmansyah, S. Triwahyono, A.A. Jaila, R.R. Mukti, E. Febriyanti, V. Suendo, H.D. Setiabudi, M. Mohamed, W. Nabgan, Oxygen vacancy-rich mesoporous silica KCC-1 for CO<sub>2</sub> methanation, *Appl. Catal. A* 532 (2017) 86–94, <https://doi.org/10.1016/j.apcata.2016.12.023>.
- [129] H. Takano, K. Izumiya, N. Kumagai, K. Hashimoto, The effect of heat treatment on the performance of the Ni/(Zr-Sm oxide) catalysts for carbon dioxide methanation, *Appl. Surf. Sci.* 257 (2011) 8171–8176, <https://doi.org/10.1016/j.apsusc.2011.01.141>.
- [130] J. Ashok, M.L. Ang, S. Kawi, Enhanced activity of CO<sub>2</sub> methanation over Ni/CeO<sub>2</sub>-ZrO<sub>2</sub> catalysts: influence of preparation methods, *Catal. Today* 281 (2017) 304–311, <https://doi.org/10.1016/j.cattod.2016.07.020>.
- [131] A.A. Alkhoori, K. Polychronopoulou, A. Belabbes, M.A. Jaoude, L.F. Vega, V. Sebastian, S. Hinder, M.A. Baker, A.F. Zedan, Cu, Sm co-doping effect on the CO oxidation activity of CeO<sub>2</sub>. A combined experimental and density functional study, *Appl. Surf. Sci.* 521 (2020) 146305, <https://doi.org/10.1016/j.apsusc.2020.146305>.
- [132] E. Santoretto, C. Novara, F. Giorgis, M. Piumetti, S. Bensaid, N. Russo, D. Fino, In situ Raman analyses of the soot oxidation reaction over nanostructured ceria-based catalysts, *Sci. Rep.* 9 (2019) 3875, <https://doi.org/10.1038/s41598-019-39105-5>.